Nanoscale Horizons

ROYAL SOCIETY OF CHEMISTRY

REVIEW

View Article Online
View Journal

Cite this: DOI: 10.1039/d5nh00844a

Emerging diverse 3D neural electrode architectures for bioelectronics

Joonho Paek,†[ab] Wonjung Park,†[ab] Hayoung Song,†[ab] Inhea Jeong,†[ab] Myoungjae Oh,†[ab] Eunmin Kim,†[ab] Dayeon Kim,†[ab] Seung Hyun An,†[ab] Younghoo Kim,†[ab] Won Gi Chung,†[ab] Sanghoon Lee,†[ab] Jongsu Lee,†[ag] Jung Ah Lim *[efg] and Jang-Ung Park *[abcde]

Received 26th December 2025,
Accepted 30th March 2026

DOI: 10.1039/d5nh00844a

rsc.li/nanoscale-horizons

Bioelectronics have been increasing in prevalence, driving extensive studies to develop systems that can perform electronic operations on various organs. In particular, neural recording technologies have undergone rapid development through the integration of advanced materials and electronic systems designed to interface directly with biological environments. Despite the developments of 1D and 2D neural interfaces, their applicability is limited by factors including elevated impedance, mechanical fragility, and poor conformability to inhomogeneous biological surfaces. To overcome these limitations, 3D neural electrodes have been extensively developed. Not only can 3D bioelectrodes enable stable interfacing with the biological surfaces, but also explore deep regions previously inaccessible with surface-based approaches. This review summarizes recent advances in 3D neural electrode architectures, highlighting their key functionalities, underlying materials and structural designs, representative applications, and current challenges.

1. Introduction

With the increasing prevalence of chronic diseases and growing societal awareness of overall health, the demand for advanced healthcare technologies continues to rise. In this context, bioelectronics has attracted significant attention as a promising approach for measuring and recording biological signals from diverse sources, including tears,[1–3] interstitial fluids,[4,5] and neural tissues.[6–8] By enabling novel functionalities such as continuous monitoring[8–10] and machine learning-assisted diagnosis,[11,12] bioelectronic devices offer new opportunities to uncover previously inaccessible information related to neural dysfunctions.[13–16]

To realize these opportunities, a broad range of emerging technologies have been introduced.[17–19] By leveraging the unique electrical, mechanical, and chemical properties of advanced materials and electronic circuits, numerous neural recording devices have been developed to improve recording efficiency and signal quality.[14,20,21] Such devices are typically designed to interface directly with biological systems, enabling *in vivo* and *in vitro* recordings from neural organs such as the brain, retina, and three-dimensional (3D) organoid models.[22,23]

A key design consideration for effective neural recording devices is dimensionality. Neural electrodes spanning one-dimensional (1D) to 3D architectures have been explored to optimize performance for specific applications.[24–26] 1D electrodes, including nanofibers and microwires, exhibit reduced motion artifacts and high adaptability to soft tissues, while 2D electrodes, such as thin films and planar arrays, offer flexibility and high spatial resolution suitable for dense electrode patterning over large areas.[27–29] However, these approaches also present limitations. 1D electrodes often suffer from elevated impedance, whereas 2D electrodes are susceptible to mechanical damage and are constrained in their ability to access deeper neural regions. Moreover, the complex geometry of the human body, where many highly curved, deformable, and continuously moving surfaces are present, poses significant challenges for maintaining long-term conformal contact with planar interfaces.

[a] Department of Materials Science and Engineering, Yonsei University, Seoul 03722, Republic of Korea. E-mail: jang-ung@yonsei.ac.kr
[b] Center for Nanomedicine, Institute for Basic Science (IBS), Yonsei University, Seoul, 03722, Republic of Korea
[c] Department of Neurosurgery, Yonsei University College of Medicine, Seoul 03722, Republic of Korea
[d] Graduate Program of Nano Biomedical Engineering (NanoBME), Advanced Science Institute, Yonsei University, Seoul, 03722, Republic of Korea
[e] Yonsei-KIST Convergence Research Institute, Seoul 03722, Republic of Korea. E-mail: jalim@kist.re.kr
[f] Soft Hybrid Materials Center, Korea Institute of Science and Technology (KIST), Seoul 02792, Republic of Korea
[g] Division of Nanoscience and Technology, KIST School, University of Science and Technology (UST), Seoul 02792, Republic of Korea
† J. P., W. P., H. S., I. J., M. O., E. K., D. K., S. H. A., Y. K., W. G. C., S. L., and J. L. contributed equally to this work.

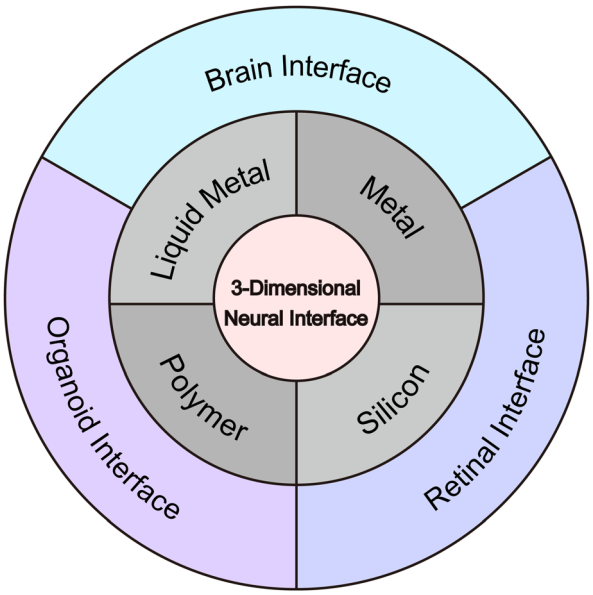

Fig. 1 Schematic illustration showing various materials and applications of 3D neural interfaces.

To address these limitations, 3D neural electrodes, including pillar structures, multilayered probes, and multielectrode arrays (MEAs), have been extensively developed.[30,31] By penetrating target tissues, 3D electrodes can achieve stable interfacing with curved and dynamic biological environments, enable tunable impedance characteristics, and access deep neural structures that are otherwise inaccessible with surface-based devices.

In this review, we highlight recent advances in 3D neural electrode architectures. We first discuss the fundamental functionalities and performance characteristics of 3D bioelectrodes, followed by an overview of the materials and structural designs employed in these systems. We then examine representative applications enabled by these architectures and conclude by addressing their advantages, current challenges, and prospective future directions in the field of 3D neural bioelectronics (Fig. 1).

2. Functionalities of 3D bioelectrodes

Biological targets of bioelectrodes, including the skin and internal organs of animals and humans, pose significant challenges for recording and stimulation due to their nonuniform and inhomogeneous interfaces. Despite these challenges, extensive studies have demonstrated that 3D bioelectrodes offer strong potential to improve interface stability and signal fidelity. This section discusses the key functional properties of 3D bioelectrodes that can be engineered to address these challenges.

2.1. Interfacial mechanisms of 3D bioelectrodes

The biointerface, which mediates communication between biological systems and artificial electronic devices, represents a critical junction between two fundamentally dissimilar domains. Conventional planar (2D) electrodes possess intrinsically limited catalytic and conductive surface areas and fail to achieve conformal contact with curved and mechanically heterogeneous biological tissues. These structural limitations lead to high interface impedance, unstable coupling under micromotion, signal distortion, and low signal-to-noise ratios (SNRs).[32] As neural and tissue-level electrophysiology increasingly demand higher spatiotemporal resolution and greater long-term stability, such shortcomings significantly restrict the performance ceiling of 2D interfaces. In contrast, 3D bioelectrode architectures overcome these structural and electrochemical constraints by introducing depth, curvature, and multiscale topographical features into the electrode–tissue interface. First, the 3D geometry enables a more conformal interaction with biological tissues, allowing the electrode to engage local microcurvatures and achieve tighter mechanical coupling compared with planar 2D electrodes (Fig. 2a). This improved geometrical matching reduces motion-induced decoupling and enhances the stability of the physical interface. Second, 3D architectures break the limitation imposed by the geometrical surface area (GSA) of planar electrodes. While 2D electrodes are constrained by their macroscopic footprint, 3D micro/nanostructures introduce roughness, porosity, and high-aspect-ratio features that substantially increase the effective surface area (ESA) (Fig. 2b). This enlarged ESA strengthens charge-transfer interactions and directly enhances the electrochemical responsiveness of the interface. Third, the high ESA of 3D structures promotes dense and deeply distributed EDL formation along micro/nanotopographical features, thereby reducing interface impedance and improving signal stability (Fig. 2c). Such volumetric ion–electrode interactions are largely inaccessible to planar systems and represent a key mechanism by which 3D designs expand the electrochemical capabilities of biointerfaces.

2.1.1. Surface area expansion and impedance reduction for recording. 3D nanostructures such as nanopillars, nanoporous metallic surfaces, and nanospikes can significantly enlarge the electrochemically active surface area without increasing the macroscopic area of the electrode. The electrical double-layer capacitance (C) increases proportionally with surface area, following the relationship $C = \varepsilon A/d$, where ε is the electrolyte permittivity, A is the ion-accessible surface area, and d represents the effective thickness of the EDL. As capacitance increases, the interface impedance (Z) decreases according to $Z \approx 1/(j\omega C)$, where j is the imaginary unit ($\sqrt{-1}$), ω is the angular frequency ($\omega = 2\pi f$), and C is the double-layer capacitance. This inverse scaling demonstrates that increasing C through 3D surface structuring directly reduces impedance.

This enhancement lowers thermal noise and improves SNR, enabling reliable detection of high-resolution electrophysiological signals. For instance, Pt-black coatings yield several-fold increases in ESA, leading to markedly reduced impedance and improved recording fidelity.[33] Nanoporous electrodes similarly achieve high-quality recordings by providing an enlarged electrode–electrolyte interface through multiscale porosity.[34]

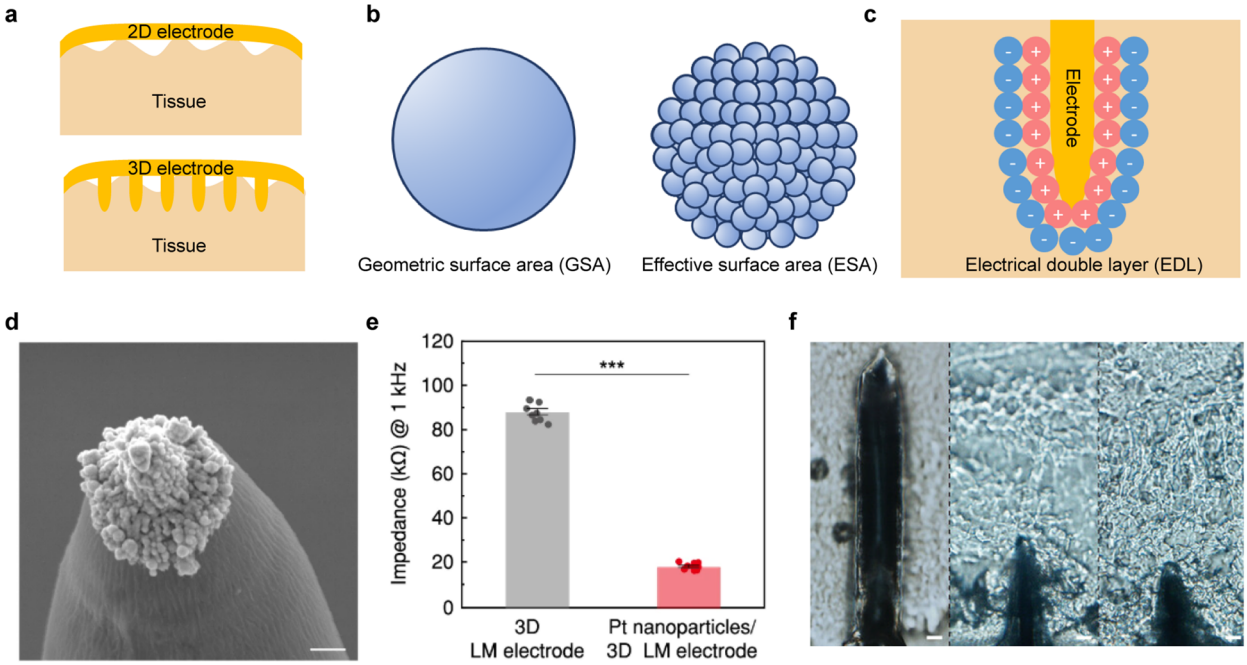

Fig. 2 Interfacial mechanisms of 3D bioelectrodes. (a) Schematic illustration of planar (2D) and three-dimensional (3D) electrodes with curved biological tissues. (b) Schematic illustration of the geometric surface area (GSA) *versus* the effective surface area (ESA) achieved through multiscale 3D micro/nanostructures. (c) Schematic illustration of electrical double-layer (EDL) formation along a 3D electrode. (d) Scanning electron microscopy (SEM) image of a liquid-metal (LM)-printed 3D micropillar functionalized with Pt nanoclusters. Scale bar, 1 μm. (e) Impedance comparison between bare 3D LM electrodes and Pt-nanocluster-functionalized 3D LM electrodes. $p = 2.27 \times 10^{-13}$. Reprinted with permission from ref. 35. Copyright 2025, Springer Nature. (f) Optical micrographs showing stable tissue contact of the 3D LM electrode under mechanical deformation, demonstrating improved electrode–tissue coupling. Scale bars, 10 μm. Reprinted with permission from ref. 40. Copyright 2024, Wiley-VCH GmbH.

Kim *et al.* further demonstrated the effect of 3D geometry and nanoscale surface engineering using liquid-metal-printed micropillars[35] (Fig. 2d). LM pillars provided enhanced 3D topography, while Pt nanoclusters selectively deposited at the pillar tips created a hierarchical roughened interface. This design produced a ~4-fold reduction in interface impedance compared with bare LM pillars (Fig. 2e). The resulting low-impedance interface enabled stable low-frequency performance essential for neural recording, illustrating how geometric and nanoscale features work together to substantially elevate recording fidelity.

2.1.2. Enhanced stimulation efficiency *via* surface area expansion. For stimulation electrodes, the ability to safely deliver sufficient charge, quantified by the charge storage capacity (CSC) and charge injection capacity (CIC), is a primary determinant of performance.[36] CSC represents the total amount of reversible charge that an electrode can store through capacitive and faradaic processes, whereas CIC defines the maximum charge that can be injected during a stimulation pulse without exceeding critical voltage limits. These metrics directly govern whether electrical stimulation remains within the safe, reversible regime or enters the region where irreversible reactions, such as water electrolysis or electrode corrosion, may occur. As extensively discussed in classical electrochemical studies, electrodes with higher CSC can sustain greater reversible charge transfer, allowing neural activation at lower voltages and reducing the risk of overstimulation-induced injury.

It should be noted that impedance, CSC, and CIC reflect different aspects of electrode performance and are most informative when interpreted according to their primary use cases. Impedance is mainly relevant to recording performance because it influences interfacial signal coupling and noise characteristics, whereas CSC and CIC are more directly associated with stimulation performance, as they reflect reversible charge handling and safe charge injection limits, respectively. In addition, these metrics are strongly influenced by measurement conditions, including frequency, scan rate, pulse width, electrolyte, electrode geometry, and normalization method. Therefore, direct quantitative comparisons across different studies should be made with caution.

3D electrode architectures inherently provide increased roughness, hierarchical porosity, and expanded electroactive surface area, enabling larger amounts of charge to be delivered under the same voltage constraints. By increasing the ion-accessible surface area, 3D structures facilitate more efficient capacitive charge storage and more distributed current flow during stimulation.[37] This reduces the local current density, mitigates overpotential, delays the onset of harmful faradaic reactions, and thereby broadens the stimulation safety window. In addition, the enhanced surface area moderates the rate of electrode degradation by distributing redox processes across a larger interface, preserving long-term functionality.

Viana *et al.* reported that nanoporous graphene electrodes further extend the benefits of 3D architectures by leveraging an

exceptionally high surface-area-to-volume ratio.[38] Their nanoporous graphene exhibited a geometric-area-normalized capacitance exceeding 10 mF cm^{-2}, approximately 10^4-fold greater than that of nonporous graphene. These findings underscore how nanostructured and porous 3D materials can simultaneously boost stimulation efficiency, reduce electrochemical stress, and promote long-term electrode stability.

2.1.3. Enhanced electrode–tissue coupling. Beyond surface area expansion, 3D electrodes improve mechanical and morphological compatibility with biological tissues, which often exhibit complex curvature and microscale topography. Structural features on similar length scales to cellular membranes allow the electrode to engage more deeply with the tissue surface, increasing physical adhesion and maximizing interfacial coupling. This enhanced contact improves seal resistance (R_{seal}), reduces current shunting around the electrode, and strengthens electrical coupling. High R_{seal} is particularly important for low-current recording conditions, where reduced background noise and mitigation of motion-induced instability are essential for maintaining signal fidelity. These structural advantages also support long-term recording stability.

Studies have shown that vertically oriented micro/nanostructured 3D electrodes provide more stable tissue engagement and superior chronic recording performance compared to planar electrodes.[39]

Lee *et al.* demonstrated that incorporating ultra-soft liquid metal into a 3D protruding microelectrode design (Fig. 2f) afforded both geometric and mechanical advantages: the 3D geometry increased interfacial engagement, while the intrinsically low elastic modulus of the liquid metal promoted conformal, mechanically compliant tissue contact.[40] This hybrid effect enabled stable electrode–tissue coupling under micromotion and supported long-term, high-quality electrophysiological recordings. These findings underscore the importance of combining structural design with mechanical compliance to optimize electrode–tissue interface performance.

2.2. In-cell recording

Cell membranes are complex assemblies of lipids and proteins that separate the cell interior from the outside environment.[41] The functions of human cells, tissues, and organs have been a major area of pursuit for study in medicine and biological sciences to understand the physiology of the human body. In particular, understanding the electrophysiology has become significant, since electrophysiology enables accurate, real-time collection of information regarding the extracellular field potentials.[42] Current extracellular multisite recordings suffer from a low SNR, limiting the monitoring to action potentials, and preclude the detection of subthreshold synaptic potentials[43,44] (Fig. 3a). These limitations complicate the analysis of neuronal networks both *in vitro* and *in vivo*.[44] Intracellular recording gives more direct information about individual neuronal properties, including the membrane potential, amplitude, duration, and rate of firing of action potentials.[45] However, probes are much more rigid than tissue and usually have dimensions substantially larger than neurons, thus often leading to significant tissue damage and degradation of recording performance.[46] Significant progress in 3D microfabrication techniques over recent decades has led to extensive research focusing on constructing 3D micro- and nanoscale bioelectrodes and probes capable of intracellular signal detection and biochemical delivery. Efforts to simultaneously record in-cell recording signals from multiple neurons in living cells by organizing vertical 3D bioelectrode arrays have advanced continuously, employing nanofabrication strategies such as lithographic patterning and 3D printing technologies.[47,48]

Hai *et al.* fabricated a submicrometer-scale, mushroom-shaped 3D microelectrode and cultured individual cells to engulf this electrode, enabling intimate cell–electrode interfacing[49] (Fig. 3b). This 62 microelectrode array facilitated multichannel recordings from multiple cells, capturing their action potentials. The following studies have demonstrated that similarly dimensioned 3D structured electrodes can closely interface with cellular membranes to gain access to the intracellular space, thereby recording in-cell action potentials effectively[49–52] (Fig. 3c). These mushroom-shaped electrodes enhance electrical coupling between neurons and the electrode by promoting membrane engulfment, which increases seal resistance and reduces extracellular voids that weaken signal quality.[53] Furthermore, nanofabrication techniques enable precise control over electrode geometry, optimizing their compatibility with mammalian neurons for stable, high-fidelity in-cell recordings over both short and long-terms.[42] Building upon the development of 3D microelectrode arrays enabling effective intracellular recordings, electroporation has emerged as a key technique to further enhance cell–electrode interfacing (Fig. 3d).[53,54] Electroporation applies brief electrical pulses to transiently permeabilize the cell membrane, allowing increased electrical access for intracellular recording while maintaining cell viability. Integration of electroporation with 3D microelectrode arrays has enabled multiplexed, high-quality intracellular recordings from various cell types, including cardiomyocytes and neurons, expanding applications in electrophysiology.[42,55] Optimizing pulse parameters such as amplitude, duration, and frequency is critical to balance efficacy and cellular health, making electroporation a versatile tool in bioelectronic interface design.[55] Recent advances have demonstrated the feasibility of combining electroporation with 3D microelectrode arrays of various dimensions fabricated using lithographic techniques, improving recording fidelity and scalability for large-scale studies.[42,56] These innovations enable the sophisticated, high-resolution bioelectronic platforms for *in vitro* and *in vivo* investigations of cellular electrophysiology.

Nanofabricated vertical 3D nanoelectrodes have revolutionized the interface between artificial bioelectronic platforms and living cells, enabling both extracellular and intracellular electrical recordings with high fidelity[57] (Fig. 3e). This illustrates a multiplexed nanoelectrode array in contact with a single cell, where electrodes fabricated by localized nanolithography or focused ion beam methods are coated with bio-interfacing metals to maximize cell adhesion and electrical coupling. Xie *et al.* present a high-resolution cross-sectional

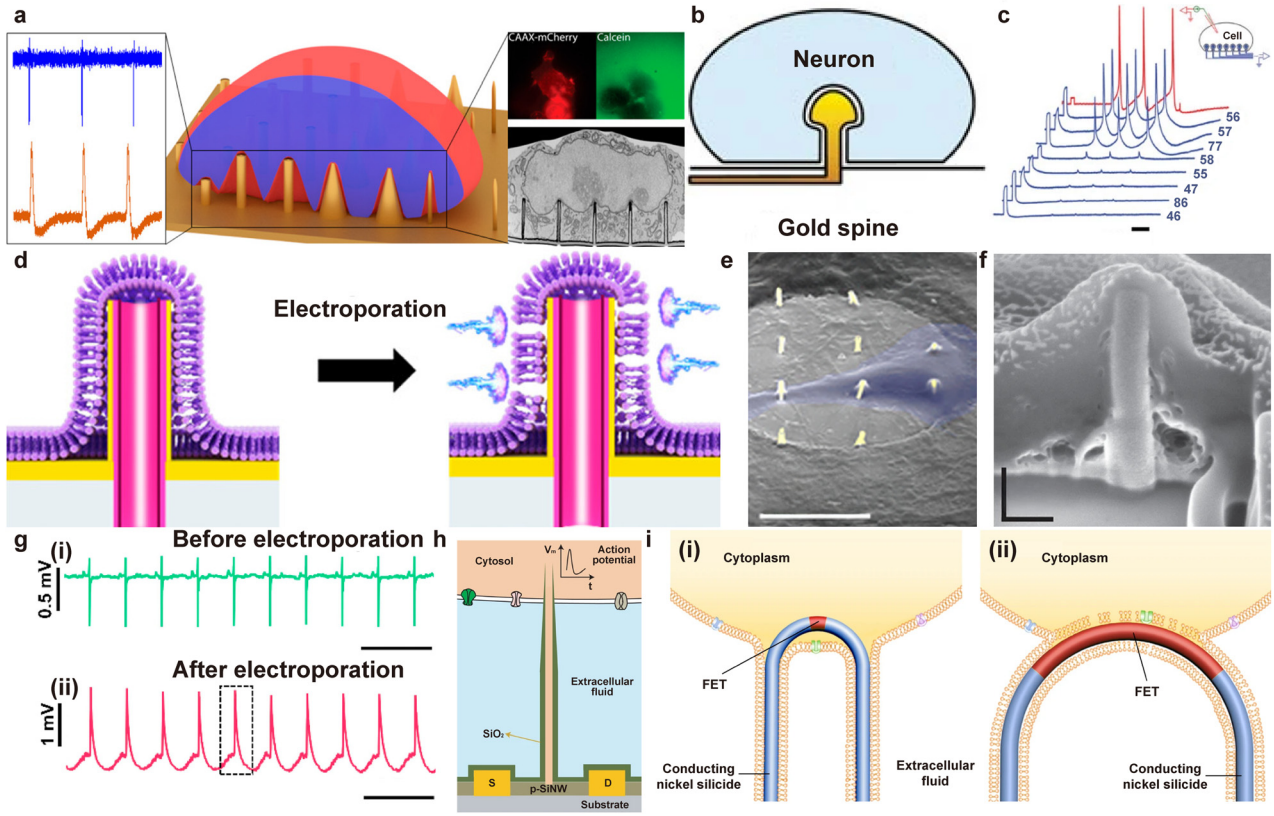

Fig. 3 In-cell recording approaches using the nanostructured interface. (a) Multifaceted characterization of the cellular membrane's mechanical stability when closely interacting with high-aspect-ratio 3D vertical nanostructures, vertical nanostructures spontaneously penetrate the cellular membrane to form a steady intracellular coupling, only in rare cases and under specific conditions. Reprinted with permission from ref. 43. Copyright 2018, American Chemical Society. (b) Schematic representations of a neuron engulfing a gold-spine electrode. Reprinted with permission from ref. 44. Copyright 2010, Springer Nature. (c) Simultaneous action potential recordings (blue) from 8 gold-spine electrodes in response to intracellular stimulation of the neuron by a conventional sharp microelectrode (red). Each trace depicts initially a 5 mV, 20 ms calibration pulse and then, after a delay, three action potentials. Inset, schematic of the experimental setup. Scale bar, 100 ms. Reprinted with permission from ref. 49. Copyright 2010, Springer Nature. (d) Schematic of electroporation on a cell membrane by a hollow nanopillar electrode. Electrical pulses generate nanopores in the cell membrane around the electrode. Reprinted with permission from ref. 53. Copyright 2022, American Chemical Society. (e) Colored SEM images of neuronal soma and processes enveloping gold plasmonic 3D nanoelectrodes. The culture was fixed at 10 div. Scale bar, 10 μm. Reprinted with permission from ref. 57. Copyright 2017, American Chemical Society. (f) The cell-nanopillar electrode interface exposed by focused ion beam milling shows that the nanopillar electrode is fully engulfed by the cell. Scale bar, 200 nm. Reprinted with permission from ref. 58. Copyright 2012, Springer Nature. (g) Action potentials recorded from cardiomyocytes before and after electroporation. (g-(i)) Extracellular action potential (EAP) recording before electroporation. (g-(ii)) Synchronized intracellular and extracellular action potential recording (IAP and EAP) after electroporation. Scale bars, 0.5 s. Reprinted with permission from ref. 59. Copyright 2019, Elsevier. (h) Schematic diagrams showing a cell coupled to a BIT-FET. S and D indicate source and drain electrodes. The SiO_2 nanotube connects the cytosol (orange) to the p-type silicon nanowire FET and, together with the SiO_2 passivation (green), excludes the extracellular medium (light blue) from the active device channel. The structures on the membrane represent different ion channels and are not scaled to the true size of the BIT-FET. Reprinted with permission from ref. 60. Copyright 2012, Springer Nature. (i) Schematics of two possible probe–cell interfaces. (i-(i)) Internalization and high-resistance seal of a short-channel U-NWFET to the cell membrane enables high-amplitude recording. The sensitive p-type Si NWFET region and the metallic NiSi region on the U-shaped nanowire are marked in red and blue-grey, respectively. The nanowire is shown modified with phospholipid. (i-(ii)) Partial sealing/internalization of the U-NWFET with longer channel length/radii of curvature results in an attenuated in-cell action potential recording. Reprinted with permission from ref. 61. Copyright 2019, Springer Nature.

scanning electron microscope (SEM) image of a vertical nanoelectrode structure that is tightly engulfed by the cell membrane (Fig. 3f).[58] The distinct topography and sharpness of these nanostructures create a local lightning rod effect, concentrating the applied electric field at the tip when a brief pulse is delivered. This concentrated field locally raises the transmembrane potential, triggering the formation of transient hydrophilic nanopores directly in contact regions. Electroporation allows the electrode to directly access the cytoplasm, resulting in an increase in recorded action potential amplitude and waveform breadth, distinguishing in-cell signals from their extracellular counterparts. Electrophysiological recordings using 3D microelectrode arrays reveal distinct differences between extracellular and intracellular signals, especially when electroporation is used to transiently permeabilize the cell membrane. Before electroporation, the recorded extracellular signal shows low amplitude and relatively narrow spikes (Fig. 3g-(i)). This signal is limited by the resistive and capacitive properties of the cell membrane, which restrict direct access to transmembrane potential changes. After electroporation, the electrode can directly

interface with the intracellular domain through the newly formed membrane pores (Fig. 3g-(ii)). The recorded signal now exhibits much higher amplitudes and broader waveforms characteristic of true intracellular action potentials. Unlike extracellular traces, these waveforms reflect the rapid depolarization and repolarization of the cell's membrane potential. This transition enables the ability of 3D electrode arrays by electroporation to obtain rich, high-fidelity in-cell signals, providing more precise insights into cellular electrophysiology compared to extracellular recordings alone.[59]

Recent advances have made it possible to achieve minimally invasive, scalable, and highly sensitive intracellular recordings using specialized field-effect transistor (FET) nanoprobes. Duan *et al.* developed a SiO_2 nanotube that integrates directly on the tip of a nanoscale FET, enabling extracellular nanodevice penetration through the plasma membrane and direct communication with the cell cytosol[60] (Fig. 3h). Once inserted, these branched intracellular nanotube FET (BIT-FET) probes record intracellular transmembrane potentials with high fidelity and bandwidth, offering broader amplitude action potentials and enabling multiplexed intracellular measurements from networks of neurons and cardiomyocytes. The unique geometry and surface chemistry of the nanotube design allow spontaneous penetration with minimal cell disruption, and a tight, stable membrane seal forms around the device, which is critical for reliable, long-term recordings. Scalable 3D nanowire transistor probes have emerged as a solution for parallelization and extremely high-density intracellular interfacing. The U-shaped nanowire FET (U-NWFET) design in particular supports multiplexed, site-selective intracellular recordings in primary neurons and dense tissue, opening the door to parallel investigations of network activity, subthreshold potentials, and cellular connectivity at unprecedented spatial resolution[61] (Fig. 3i). Importantly, these devices enable high SNR ratios, faithfully tracking diverse electrophysiological signatures and subthreshold signals that are inaccessible to standard extracellular platforms. These FET innovations in nanoscale bridge the gap between the invasiveness of patch-clamp and the limitations of extracellular field recordings, delivering reproducible, full-bandwidth in-cell signals of cellular electrophysiology.

3. Materials and structures of 3D bioelectrodes

3D bioelectrodes employ a wide range of materials and structural designs. As these devices are typically implanted within the body, their development must account for critical factors such as biocompatibility, mechanical compliance and motion artifacts.[62] This section discusses the materials and structural strategies used in 3D bioelectrodes and how they enable the desired device functionalities.

3.1. Metal-based 3D electrode

Metals are the predominant electrode materials in bioelectronics and neural interfaces owing to their high electrical conductivity and electrochemical stability.[63–65] To translate these materials into 3D electrode architectures, several design strategies have been pursued: (i) structuring the substrate itself in 3D and subsequently depositing metal to form 3D electrodes; (ii) engineering the electrode architecture so that multiple spatially distributed neural signals can be recorded within a 3D volume; and (iii) introducing 3D nanoporosity *via* electrochemical deposition to tailor the surface roughness and pore morphology of the metallic electrode. In this section, we focus specifically on strategies in which the metal itself is used to define the 3D electrode structure. The following examples should be interpreted with the understanding that impedance primarily informs recording characteristics, whereas CSC and CIC are more directly associated with stimulation performance.

3.1.1. Geometry-engineered 3D metal electrode. A variety of strategies have been developed to realize 3D metal electrodes. Beyond simply stacking multiple metal layers, geometric engineering of the electrode layout can be used to construct intrinsically 3D architectures.[8] In particular, mesh-like metal electrodes provide a powerful route to transform otherwise rigid metal structures into highly stretchable and flexible interfaces. Such mesh architectures can be delivered through a minimally invasive injection footprint and subsequently unfold within the tissue, thereby achieving high recoding density over a large 3D volume while minimizing insertion damage. Owing to their open, compliant geometry, mesh electrodes induce markedly reduced tissue damage and foreign-body response, enabling stable long-term device operation.

Leveraging these advantages, Sheng *et al.* positioned an ultraflexible mesh electrode onto the neural plate at the surface of a frog embryo, allowing the mesh to deform and expand concomitantly with neurulation and brain development to form a 3D neural interface.[66] As shown in Fig. 4a, the recording sites were defined by 40 nm-thick Pt electrodes, while the interconnects consisted of 50 nm-thick Au traces patterned in a serpentine ribbon geometry to preserve structural integrity during 3D deployment. The metallic network was encapsulated with a perfluoropolyether-dimethacrylate (PFPE-DMA) layer, whose elastic modulus is approximately five orders of magnitude lower than that of SU-8 yielding an extremely soft 3D metal electrode. Owing to this mechanically compliant design, the mesh maintained stable electrical conductivity even under 33% longitudinal strain (Fig. 4b). This mechanical robustness translated directly into electrochemical stability, with the electrodes exhibiting stable impedance values *in vivo* for at least 7 days after implantation into the embryo (Fig. 4c).

Building on this mesh-based architecture, Lee *et al.* demonstrated simultaneous recording from multiple brain regions across the left and right hemispheres using a single metal mesh electrode.[67] A similar mesh design with 50 nm-thick Pt electrodes and 100 nm-thick Au interconnects was loaded into sterile saline and injected through a capillary needle, enabling sequential stereotaxic delivery into multiple targets. This procedure was first validated in a brain-like hydrogel phantom (Fig. 4d). After optimization, the approach was applied *in vivo* to access four regions spanning the left and right hippocampi

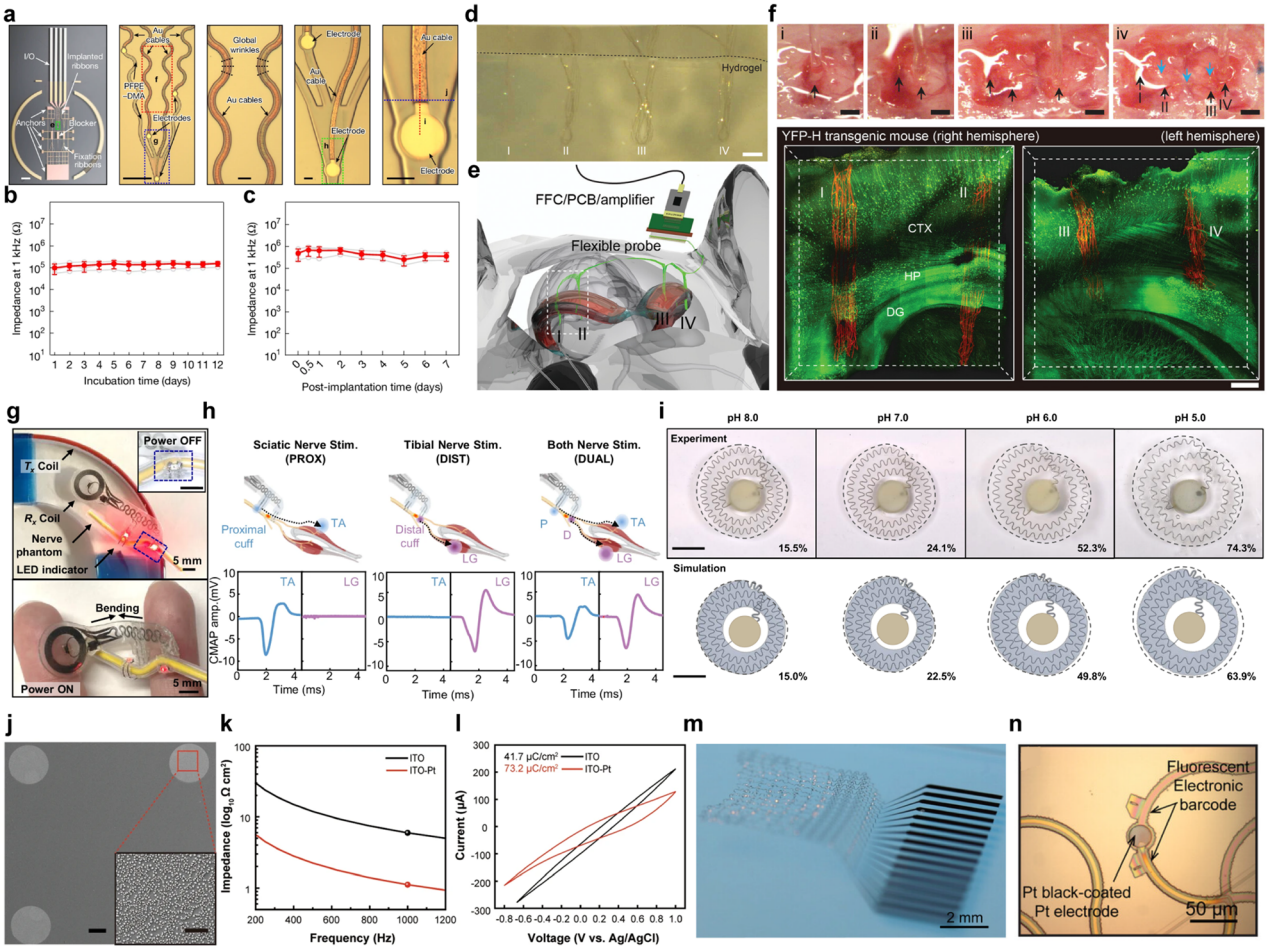

Fig. 4 Approaches and characteristics of metal-based 3D neural electrodes. (a) Bright-field microscopic images of PFPE-DMA mesh electronics on a glass substrate. Scale bars: 1 mm, 100 μm, and 10 μm. (b) PFPE-DMA mesh electrode's impedance at 1 kHz throughout 12 days incubation in 37 °C PBS. (c) PFPE-DMA mesh electrode's impedance throughout 7 days post-implantation. Reprinted with permission from ref. 66. Copyright 2025, Springer Nature. (d) Optical microscopic image of a single flexible probe stitched into agarose hydrogel's 4 different regions. Scale bar, 3 mm. (e) Schematic illustration of 4-site implantation of a single flexible probe stitched across the mouse brain. (f) Optical microscope image of a single flexible probe stitched to 4 different sites of the mouse hippocampal region (top). Scale bars, 500 μm, and 3D mapping of the flexible probe implanted across left and right hemisphere of mouse brain (bottom). Reprinted with permission from ref. 67. Copyright 2023, Wiley-VCH GmbH. (g) Photographs of a bioresorbable nerve stimulator device integrated with a phantom nerve (top), and placed between fingers (bottom). (h) Schematic illustration of experimental set-up (top) and CMAP signals recorded from tibialis anterior (TA) and lateral gastrocnemius (LG) muscles. Reprinted with permission from ref. 69. Copyright 2025, Springer Nature. (i) Experimental (top) and simulation result (bottom) of a bioresorbable pH sensor exposed to 4 different pH environments after 2 hours. Reprinted with permission from ref. 70. Copyright 2024, The American Association for the Advancement of Science. (j) SEM image of the stimulating electrode deposited with Pt nanoclusters. Scale bars: 200 μm and 8 μm (inset). (k) Impedance of the pristine ITO electrode and ITO-Pt electrode over 200 to 1200 Hz. (l) Cyclic voltammetry graph of the pristine ITO electrode and ITO-Pt electrode recorded at a sweep rate of 100 mV s^{-1}. Reprinted with permission from ref. 71. Copyright 2024, Springer Nature. (m) Optical microscope image of stretchable mesh nanoelectronics floating in saline solution. (n) Bright-field microscopic image of the stretchable mesh nanoelectronics' electrode coated with Pt black. Reprinted with permission from ref. 72. Copyright 2022, Wiley-VCH GmbH.

with a single probe (Fig. 4e). Following injections at each site, the mesh electrode was found to interpenetrate through the cortex (CTX) and extend into the hippocampus (HIP) and dentate gyrus (DG), confirming that geometrically engineered mesh metal electrodes can form conformal 3D neural interfaces across distributed brain structures (Fig. 4f).

Similar to mesh-structured electrodes, serpentine interconnect geometries represent another widely adopted strategy to impart large stretchability and out-of-plane deformability to otherwise rigid metal electrodes.[1,68] By allowing the metal traces to buckle, twist and unfold under strain, these serpentine layouts enable 3D deployment of metallic neural interfaces while preserving electrical continuity. Ahn *et al.* developed a fully bioresorbable, wirelessly powered peripheral nerve stimulator in which a single 15-μm thick Mo sheet is laser-cut to define the Rx coils, serpentine-structured extension leads, and cuff electrodes, thereby enhancing mechanical robustness and electrical continuity compared with bonded multilayer designs[69] (Fig. 4g). The nerve–electrode interface is implemented using two cylindrical cuff electrodes that wrap circumferentially

around the nerves, forming a 3D coaxial contact geometry rather than a planar pad. The proximal cuff is mounted on the sciatic nerve trunk, whereas the distal cuff is placed on the tibial nerve branch. Both cuffs are electrically connected in parallel to the same Rx-rectifier module but can be selectively engaged (proximal only, distal only, or both) by configuring the extension-electrode connections. This cuff-type 3D architecture enables intimate circumferential contact with the nerve fascicles, efficient current delivery at low voltages (3–5 V at 50 Hz), and stable mechanical fixation during chronic implantation. Its stimulation capability was demonstrated *via* selective activation of the sciatic and tibial nerves, as confirmed by compound muscle action potentials (CMAPs) recorded in the tibialis anterior (TA) and lateral gastrocnemius (LG), depending on the 3D cuff-connection configuration (Fig. 4h).

Similarly, Li *et al.* reported a fully bioresorbable wireless pH sensor in which a geometrically engineered 3D metal inductor is mechanically coupled to a pH-responsive hydrogel to transduce gastric acidity into an inductive signal.[70] The device consists of a filamentary serpentine planar spiral coil laser-cut from 100-μm thick Zn foil, which serves as the inductor (L), and a parallel-plate capacitor (C) formed by a PLGA dielectric film sandwiched between Zn electrodes; together, these components are integrated into a compact LC resonant circuit. The Zn inductor is conformally coated with a thin bioresorbable wax layer and embedded within a poly[2-(diisopropylamino)-ethyl methacrylate] and poly(ethylene glycol)diacrylate (PDPAEMA–PEGDA) hydrogel disk, whereas the capacitor is separately encapsulated in a wax shell and connected to the inductor *via* a bioresorbable tungsten wax conductive paste, yielding a soft, flexible construct that can be sutured near the gastric staple line for postoperative monitoring. The key 3D functional element is the hydrogel-encased spiral inductor. Below the hydrogel's pK_a ($\sim$6.3), protonation of tertiary amine groups induced strong electrostatic repulsion and osmotic swelling, driving substantial radial expansion of the hydrogel and the embedded serpentine coil. As portrayed in Fig. 4i, the sensor area increases from $\sim$15–25% at pH 8.0–7.0 to $\sim$50–75% at pH 6.0–5.0, accompanied by pronounced out-of-plane buckling and in-plane unfolding of the Zn traces. This pH-dependent geometric deformation increases the effective inductance L; when the variable inductor is wired in series with the fixed capacitor, the LC resonance frequency shifts as a function of pH. In this way, a 3D deformable metal inductor-electrode, whose geometry is actively reconfigured by the surrounding hydrogel, encodes local pH into a wireless inductive signal, providing a representative example of a structurally reconfigurable 3D metal electrode architecture for implantable biosensing.

3.1.2. Electrodeposition-enabled 3D microstructure metal electrodes. Electrodeposition offers a powerful route to transform nominally planar metal electrodes into 3D nanostructured interfaces by selectively growing nanostructured Pt on the electrode surface. This geometry-driven increase in effective surface area leads to pronounced reductions in 1 kHz impedance and substantial enhancements in CSC and CIC, thereby markedly improving the overall electrochemical performance of neural electrodes.

Lim *et al.* enhanced the efficiency of electrotactile stimulation by electroplating 3D Pt nanostructures referred to as 'Pt black' on transparent ITO electrodes.[71] The electrotactile actuator consists of a 10 × 10 array of circular ITO pads (100 nm thick, 500 μm diameter) patterned on a colorless polyimide (PI) substrate, where Pt nanoclusters are electrodeposited onto the ITO surface to increase the effective interfacial area while preserving high optical transmittance ($>$89% in the visible range). SEM images in Fig. 4j reveal a dense, rough Pt nanocluster layer conformally covering the ITO, forming a 3D microstructured metal surface. This morphology substantially reduces the electrode impedance: at 1 kHz, the Pt-coated ITO (ITO-Pt) exhibits an impedance of 1.11 Ω cm^2 compared with 5.95 Ω cm^2 for pristine ITO ($\sim$5-fold reduction), and maintains approximately fourfold lower impedance even after 70 min of repeated electrical stimulation (Fig. 4k). Furthermore, cyclic voltammetry measurements show that the CSC increases from 41.7 to 73.2 μC cm^{-2} after Pt deposition (Fig. 4l), confirming that electrodeposition-enabled 3D Pt nanostructures markedly improve both the charge-transfer capability and long-term electrochemical stability of transparent electrotactile electrodes.

As another implementation, Le Floch *et al.* employed Pt black-modified Pt electrodes to ensure long-term, low-impedance recording in their stretchable mesh nanoelectronics designed for 3D brain organoid electrophysiology (Fig. 4m).[72] The mesh architecture comprises 25-μm-diameter Pt electrodes (50 nm thick) patterned on 40 nm Au interconnects and encapsulated within 800 nm SU-8 layers, where the electrode surfaces are electroplated with Pt black to form a highly rough, 3D nanostructured interface (Fig. 4n). The Pt-black coated electrodes exhibit an initial impedance of 1.40 ± 0.50 × 10^5 Ω at 1 kHz, which only modestly increases to 3.00 ± 0.33 × 10^5 Ω after 180 days of incubation in PBS at 37 °C, thereby maintaining low noise levels ($<$15–20 μV) during chronic recording.

3.2. Silicon

Silicon has long been a foundational material in both the semiconductor and bioelectronics industries, serving not only as a structural substrate but also as an active electrode material.[73,74] Its versatility arises primarily from the spontaneous formation of a stable native oxide (SiO_2) layer upon exposure to air, which provides excellent chemical passivation, biocompatibility, and electrical insulation. This naturally-formed oxide enables silicon-based devices to interface safely with biological tissues while maintaining long-term stability under physiological conditions.

Beyond its favorable surface chemistry, silicon's mechanical rigidity and compatibility with mature microfabrication processes have made it the cornerstone for constructing high-resolution and geometrically precise neural interfaces. Silicon wafers allow the use of advanced microelectromechanical system (MEMS) fabrication techniques such as photolithography and deep reactive ion etching (DRIE), which enable the formation of complex, high-aspect-ratio 3D structures. These processes allow precise control

over shank geometry, electrode spacing, and integration of multiple functional layers.[75–77]

3.2.1. Shank-type neural probes. Shank-type neural probes represent one of the most significant outcomes of silicon micromachining in neural engineering.[78] These probes are thin, blade-like structures designed to penetrate brain tissue and record neuronal activity across different depths. Their small footprint minimizes tissue displacement during insertion while enabling multi-site recording across cortical and subcortical regions. The well-known Michigan-type probe is a representative example of this approach, fabricated through anisotropic DRIE of silicon wafers followed by metallization and passivation.[79] This structure provides a platform for integrating hundreds of recording sites within a compact cross-sectional area while maintaining structural stiffness sufficient for insertion through the dura.

More recently, silicon neural probes have been developed with significantly increased channel density and recording area by extending the probe shank length and incorporating on-chip multiplexing circuitry. Trautmann *et al.* reported the development of Neuropixels 1.0 NHP, which utilizes a 45 mm-long silicon shank populated with 4416 recording sites fabricated using 130 nm complementary metal–oxide–semiconductor (CMOS) lithography[80] (Fig. 5a). Compared with earlier 10 mm versions designed for small-animal models,[81] this extended probe enables large-scale, simultaneous recordings throughout deep brain regions of nonhuman primates (NHPs). The use of silicon enables such scalability because it maintains high structural integrity while allowing precise patterning of microelectrodes and embedded interconnects through standard wafer-level processing.

In addition to electrical recording, extensive research has focused on expanding the functional versatility of silicon probes. Multifunctional probe architectures now integrate microfluidic channels, optical waveguides, and temperature sensors within the same silicon backbone. For instance, Shin *et al.* demonstrated a silicon-based MEMS neural probe capable of simultaneous electrophysiological recording, optical stimulation, and localized drug delivery.[82] The microchannels for fluidic transport were fabricated alongside the electrode shank *via* photolithography and DRIE, forming internal capillaries for precise delivery of pharmacological agents (Fig. 5b). Such integration allows the modulation and recording of neural activity in real time, enhancing the ability to investigate interregional connectivity and neuromodulation mechanisms.

3.2.2. Array-type electrodes. Different from the Michigan-style probe, which consists of a single or a few slender shanks designed to penetrate vertically into brain tissue, the Utah array is composed of a dense grid of multiple penetrating electrodes projecting from a common base.[83] Developed by Normann *et al.*, the array typically contains 100 silicon electrodes, each approximately 1.5 mm in length and spaced about 0.4 mm apart (Fig. 5c). This three-dimensional configuration allows simultaneous interaction with neurons distributed across a

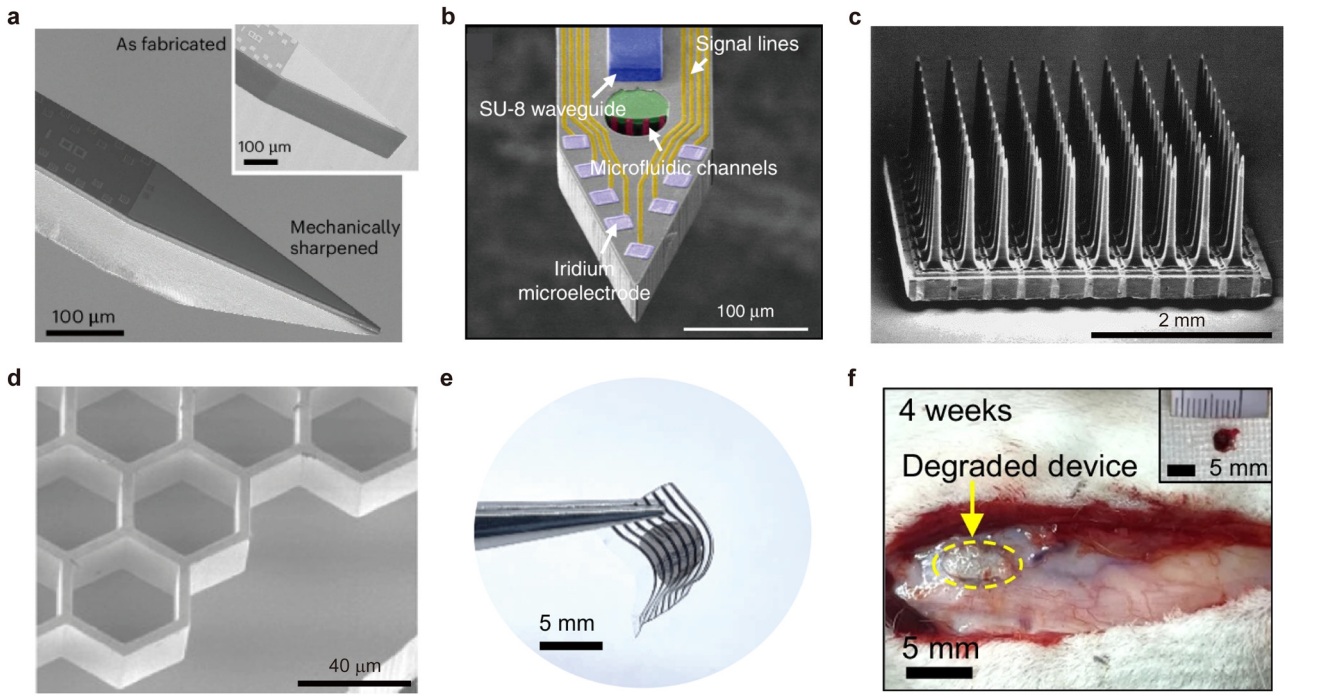

Fig. 5 Silicon-based structures for neural interfacing. (a) SEM image of the Neuropixels 1.0 NHP probe tip after mechanical grinding. Inset, probe tip before grinding. Reproduced with permission from ref. 80. Copyright 2025, Springer Nature. (b) Colorized SEM image of the multifunctional MEMS neural probe tip. Reproduced with permission from ref. 82. Copyright 2019, Springer Nature. (c) SEM image of a Utah array with 100 microelectrodes. Reproduced with permission from ref. 83. Copyright 1999, Elsevier. (d) SEM image showing the honeycomb microstructure of the PRIMA subretinal implant. Reproduced with permission from ref. 85. Copyright 2025, Springer Nature. (e) Photograph of a biodegradable optoelectronic device. (f) *In vivo* degradation of the silicon-based optoelectronic device. Reproduced with permission from ref. 88. Copyright 2024, Springer Nature.

broader cortical surface and depth, making it particularly effective for stimulating large neural populations or mapping complex cortical regions. The Utah array's geometry therefore provides a powerful platform for both large-area neural stimulation and high-density parallel recordings.

Similar to the Utah array's array-based architecture, Bhuckory *et al.* developed next-generation arrays of the subretinal photovoltaic implant known as PRIMA, designed for visual prosthetic applications.[84,85] The upgraded implants introduced honeycomb and pillar-type geometries to enhance electrical field penetration and improve retinal integration, ultimately achieving higher visual acuity. The honeycomb configuration features 25–30 μm tall isolating walls surrounding each pixel, guiding bipolar cells to migrate into the cavities and align with the vertical electric field, thereby lowering stimulation thresholds. In contrast, the pillar design elevates active electrodes toward the inner nuclear layer for closer neuronal contact. Both architectures represent significant advancements over the planar PRIMA design with 100 μm pixels, enabling pixel sizes down to 22 μm while maintaining retinal health and excitability. Fig. 5d shows the SEM image of the PRIMA device featuring the honeycomb array structure.

3.2.3. Porous electrode architectures. Silicon's intrinsic photovoltaic properties enable its use as a light-responsive material for wireless bioelectronic stimulation, eliminating the need for physical leads or external wiring. Li *et al.* demonstrated a monolithic silicon membrane capable of photoelectrochemical stimulation, utilizing a porosity-based heterojunction to achieve localized photocurrent generation.[86] The nanoscale porous architecture was fabricated through a combination of metal-assisted chemical etching (MACE) and stain-etching, enhancing carrier confinement and establishing interfacing band bending that facilitates efficient charge separation across the junction. This architecture allows light pulses to induce transient anodic and cathodic currents on the same silicon surface, creating inherently charge-balanced stimulation suitable for safe bioelectronic operation.

3.2.4. Dimensional tuning for biodegradability. Silicon can also function as a biodegradable electrode when its dimensions are tuned to achieve controlled hydrolysis within a desired time frame.[87] Sun *et al.* developed a biodegradable and flexible silicon-based neural interface that enables transdermal optoelectronic modulation and promotes peripheral nerve regeneration[88] (Fig. 5e). The device consists of a 2.5 μm-thick Si p–n diode integrated on a flexible polymer substrate, with a dissolvable molybdenum interfacial layer to enhance charge injection. Upon illumination with red light, the interface generates biphasic photocurrents capable of stimulating peripheral nerves while gradually dissolving in physiological environments, thereby eliminating the need for device retrieval and minimizing infection risks (Fig. 5f).

3.3. Polymer

Conventional neural interfaces rely on planar (2D) electrodes, which bias recordings toward surface-proximal signals[89] and cause mechanical mismatch and long-term stability[90] by using rigid materials such as silicon and metals. To mitigate these limitations, polymer-based platforms with low Young's modulus should be adopted to enhance tissue compliance, and electrode architectures should be designed in 3D to capture depth-resolved information.[91,92] 3D architectures reduce contact impedance, expand the effective contact area, and enable broader and more uniform access to target circuits.[93] In this section, we introduce polymer-centric 3D electrode architectures, including cuff structures, kirigami structures, pillar structures, spheroid-wrapping structures, and stretchable microneedle structures.

3.3.1. Cuff Structure. Traditional nerve cuffs are relatively thick or essentially 2D, which increases surgical difficulty and the risk of nerve damage, and they have limited adaptability to changes in nerve diameter and position.[94,95] To address this, Dong *et al.* proposed an electrochemically actuated cuff that integrates a PPy(DBS)/Au-parylene C bilayer actuator on an ultrathin parylene C (PaC) laminate together with poly(3,4-ethylenedioxythiophene):polystyrene sulfonate (PEDOT:PSS) recording electrodes.[96] Actuation relies on volumetric expansion and contraction of PPy(DBS) driven by ion injection and expulsion, enabling fast, reversible bending under sub-volt operation to actively control cuff diameter. By arranging the actuator strips, both gentle pinching and spiral self-wrapping are achieved, supported by the very low bending stiffness of the PaC laminate (21 Pa mm^3). When actuators are aligned parallel to the electrode direction, out-of-plane bending is suppressed and a minimum bending radius of 170 μm is achieved; an asymmetric layout enables rapid four-turn spiral deployment within 2.09 s (Fig. 6a). The recording electrodes are Ti/Au coated with PEDOT:PSS, giving 1 kHz impedance of 4.1 ± 0.4 kΩ in phosphate-buffered saline (PBS) with only minor change after 1000 large-deformation bending cycles. *In vivo* experiments on the rat sciatic nerve demonstrated that the cuff could be unfolded and positioned adjacent to the nerve under −0.5V. Upon removal on the voltage, the device autonomously self-wrapped around the nerve, enabling stable recording of stimulation-locked spikes, and subsequent reverse actuation allowed gradual opening of the cuff for removal with minimal tissue disruption.

3.3.2. Kirigami structure. To access three-dimensional neural circuits, various 3D MEAs such as Utah and Michigan-style arrays have been developed to record across layers and regions. However, the mechanical mismatch of these rigid silicon-based probes often elicits foreign-body responses and progressive degradation of recording quality in chronic settings.[97,98] Kirigami-based transformations address these limitations by enabling out-of-plane reconfiguration on flexible polymer films. Jung *et al.* converted a planar PaC-based MEA into a 3D probe by parallel lifting of designed kirigami cuts using matched dies, followed by thermoforming to fix 90° standing angles, thereby co-locating surface and penetrating electrodes on a single flexible substrate[99] (Fig. 6b). The design space includes shank heights of 225–1000 μm, inter-shank spacing down to 50 μm, and up to 128 shanks per probe. PEDOT electroplated on Au reduced the average 1 kHz impedance to

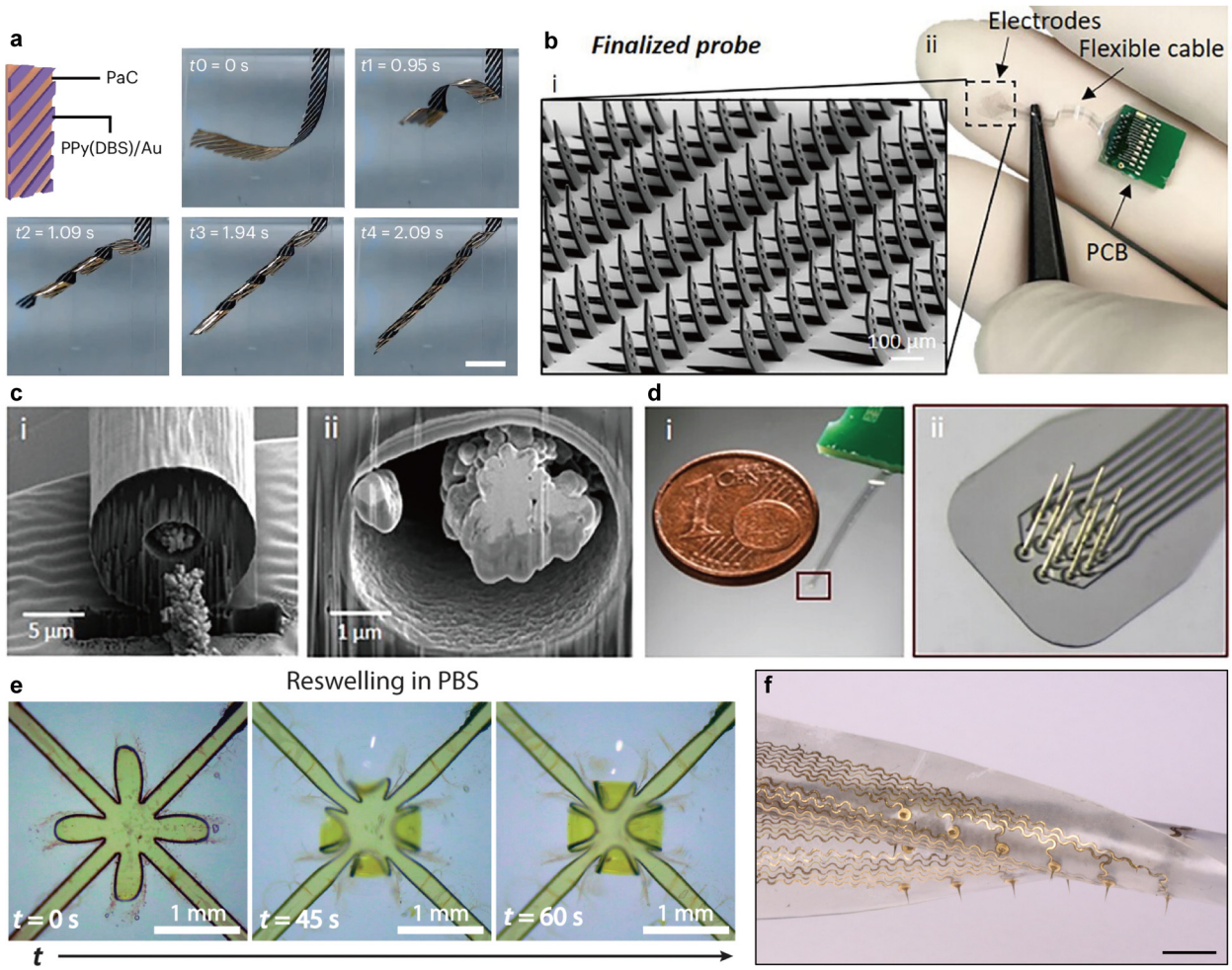

Fig. 6 Polymer-based 3D electrode structures for neural recording. (a) Electrochemically actuated, self-wrapping nerve cuff based on a PPy(DBS)/Au-parylene C bilayer actuator integrated on an ultrathin parylene C laminate. Scale bars, 1 mm. Reprinted with permission from ref. 96. Copyright 2024, Springer Nature. (b-(i)) SEM image of the kirigami-transformed 3D probe array. (b-(ii)) Photograph of the device integrated with a PCB and a flexible cable. Reprinted with permission from ref. 99. Copyright 2025, John Wiley & Sons. (c) Focused ion beam (FIB)-cut cross-sections of a hollow polymer pillar electrode. (c-(i)) Cross-section near the base. (c-(ii)) Cross-section near the top. (d) Flexible 3D MEA with polymer pillar electrodes. (d-(i)) Overview of the 3D MEA. (d-(ii)) Magnified view of a 500-µm-tall pillar electrode. Reprinted with permission from ref. 100. Copyright 2024, John Wiley & Sons. (e) Time-lapse images of a PI-PAA "e-Flower" wrapping MEA that self-closes during reswelling in PBS to achieve conformal 360° coverage of a spheroid. Reprinted with permission from ref. 103. Copyright 2024, American Association for the Advancement of Science. (f) Stretchable microneedle electrode array under stretching and twisting. Scale bars, 3 mm. Reprinted with permission from ref. 104. Copyright 2024, American Association for the Advancement of Science.

39.1 ± 3.4 kΩ, and straight feedlines showed lower process variability than meanders. Buckling analysis and agarose insertion tests confirmed unsupported insertion up to 530 µm. Functionally, local network activity was decomposed in brain slices, and in acute and chronic mouse cortex experiments, layer-dependent spatial activity was mapped with simultaneous surface and penetrating recordings. The key contribution is a wafer-scale framework that rapidly and uniformly converts flexible films into vertically integrated 3D arrays without slow manual assembly or high-aspect-ratio beam-bending steps.

3.3.3. Pillar structure. Silicon Utah-style arrays offer configurable 2D/3D needle layouts and adjustable heights but require multiple dry/wet etches and wafer bonding, creating substantial fabrication burden, and they still face limits in lowering bending stiffness for chronic use. To overcome the limits of silicon Utah-style arrays, Abu Shihada *et al.* used two-photon polymerization (2PP) to print hollow polymer pillars with a thin doughnut-shaped base for adhesion and sealing, then electroplated Au inside the pillars and electrochemically deposited PEDOT:PSS on the tips to reduce impedance.[100] Cross-sections show a polymer template that is thicker at the base and thinner near the tip, with Au uniformly filling the lumen and a thin capped tip (Fig. 6c). The approach is compatible with rigid SU-8 or quartz and with flexible PaC; tapered wall-thickness designs enabled unsupported insertion of 190 µm. The 1 kHz impedance decreased from 1.2 MΩ to 35.2 kΩ after tip capping, and a flexible 3D MEA example with 500 µm tall pillars is shown (Fig. 6d). The design affords

freedom in height, diameter, pitch, and tip geometry; buckling limits and Johnson–Nyquist noise were quantified to support insertability and signal quality. Functionally, spiking of neurons cultured on a 3D scaffold was recorded; light-evoked increases in local field potentials (LFPs) and spiking were observed in rat retina explants; and acute mouse cortex insertions showed depth-dependent spike amplitudes with 0.5–1 ms delays. In summary, the polymer template serves as both an electrode-growth channel and a mechanical support, decoupling 3D form from silicon micromachining while providing low-impedance metallic tips; the throughput of serial 2PP remains a bottleneck for ultra-large arrays.

3.3.4. Wrapping structure. Recent buckling-type flexible MEAs often require specific solvents[101] and custom wiring harnesses,[72,102] limiting practical use. Martinelli *et al.* developed a polyimide-polyacrylic acid (PI-PAA) bilayer that generates programmed curvature *via* anisotropic swelling upon rehydration, enabling a petal-shaped film to self-close from 2D to 3D and achieve 360° wrapping of cortical spheroids as an "e-Flower"[103] (Fig. 6e). The electrode layer comprises thirty-two circular platinum (Pt) sites (30 μm diameter) formed on PI and passivated with PI except for openings. PAA is wafer-level grafted onto PI *via* covalent bonding after 15 nm SiO_x activation, and petals and hinges are patterned by femtosecond-laser micromachining. Closure is induced in aqueous medium without added solvent or mechanical actuators and is reversible for at least three cycles. The radius of curvature at 37 °C is tuned to 300 μm to accommodate 500–1000 μm spheroids. The 1 kHz impedance remains similar between planar and closed states (representative 327.7 kΩ). In operation, a one-year-cultured spheroid placed on the open flower closes within minutes; after about 8 h stabilization, spontaneous field potentials across the spheroid surface are recorded and mapped. The device covers the full curved surface without destructive embedding or complex hardware, and PI/hydrogel thickness, petal count, and channel count can be adjusted to the application.

3.3.5. Microneedle structure. Achieving minimally invasive, high-resolution deep-tissue recordings requires stretchable 3D MEAs, yet penetrating-electrode fabrication typically relies on high-modulus materials that limit device compliance. Zhao *et al.* proposed a stretchable microneedle electrode array to overcome this incompatibility[104] (Fig. 6f). Conical cavities were laser-machined in PDMS and replica-molded to form conical PI needle cores; Cr/Au interconnects were patterned on a thin PI layer; and parylene insulation was applied with selective tip openings. The array was built on a 200 μm Ecoflex 00-30 substrate using PI-Ti/SiO_2-Ecoflex bonding to suppress delamination. The needle length (0.5–2 mm), base diameter (300–800 μm), and tip diameter (10–30 μm) are tunable. After tip opening, electroplated platinum black (Pt black) reduced the 1 kHz impedance from 66 kΩ to 1.6 kΩ. Impedance changed minimally up to 40% tensile strain and increased at 60–90% while maintaining function. In an *Aplysia* buccal-mass *ex vivo* model, an 8-channel array aligned with muscle fibers and inserted into I1/I3 and I2 muscles enabled simultaneous intramuscular EMG through contraction–relaxation-rest phases. Power spectra concentrated near 5–20 Hz, with higher amplitude and selectivity than a thin surface MEA under identical conditions; array stretchability preserved contact stability during motion, improving the SNR.

3.4. Liquid metal

Despite recent advances in soft electrode technologies, solid-based electrodes inevitably exhibit a mechanical mismatch with biological tissues, which inherently exhibit low elastic modulus. In contrast, liquid metals remain in a fluid state at room temperature due to their low melting points while retaining the high electrical conductivity characteristic of metals. These materials combine tissue-like mechanical compliance with excellent electrical performance, making them highly suitable for minimizing tissue damage and enabling precise neural recording and neuromodulation.[105] Among them, gallium-based liquid metals such as EGaIn (eutectic gallium indium, 75% Ga, 25% In) and galinstan exhibit relatively low toxicity and favorable biocompatibility, supporting their safe use *in vivo* and contributing to their broad adoption in bioelectronic systems.[106–108]

Furthermore, biological tissues undergo frequent repetitive and large deformations, necessitating electrode materials that can operate stably even under such mechanical conditions. Liquid metals exhibit both high stretchability and self-healing properties after damage, enabling them to maintain electrical continuity even in environments with repeated deformation.

3.4.1. Cuff structure. This liquid metal, characterized by high stretchability and deformability, enables the realization of 3D structural configurations, such as cuff-type electrodes. Consequently, such electrodes can conform to complex biological structures, including peripheral nerves, while maintaining stable electrical performance. For instance, Guo *et al.* fabricated a soft neural electrode with a multilayer liquid metal-PDMS architecture by spraying atomized EGaIn onto a PDMS substrate through a stainless steel mask, followed by encapsulation with a second PDMS layer.[109] The resulting electrode exhibited a tissue-like low elastic modulus of approximately 1.05 MPa. Fatigue testing demonstrated that the liquid metal interconnects maintained stable resistance ($\sim$4 Ω) even after more than 7000 deformation cycles at 15% strain. In preliminary experiments, these electrodes were applied to stimulate the sural and tibial nerves of a dead bullfrog, showing superior conductive performance compared to platinum due to their excellent mechanical compliance (Fig. 7a). Building upon the short-term nerve stimulation and connectivity demonstrated in the dead bullfrog model, Tang *et al.* further advanced the approach by developing a galinstan-based fluidic cuff electrode capable of long-term peripheral nerve recording and stimulation in freely moving rats[110] (Fig. 7b). This chronic application was facilitated by the liquid metal electrode's high deformability, tissue-compatible mechanical properties, and stable electrical performance under repeated dynamic strain. These findings highlight that liquid metal electrodes can achieve structurally conforming 3D configurations, such as cuff-type geometries, and provide a critical foundation for the development of

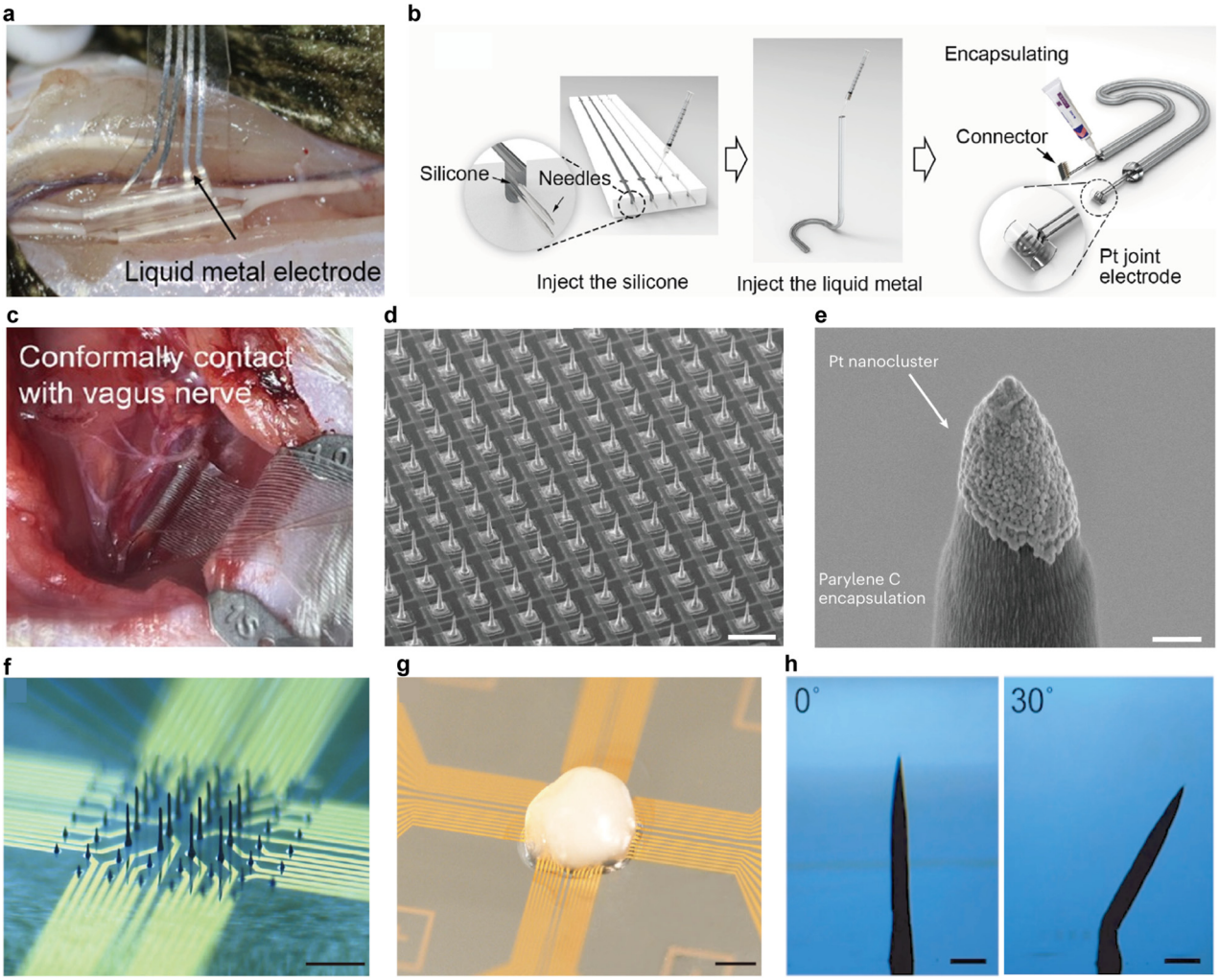

Fig. 7 Liquid metal electrodes. (a) Photograph of the implanted liquid metal electrodes interfacing with the sural and tibial nerves of a bullfrog. Reprinted with permission from ref. 109. Copyright 2017, Institute of Physics Publishing. (b) Schematic illustration of the liquid metal cuff electrode. Reprinted with permission from ref. 110. Copyright 2022, Elsevier. (c) Photograph of a self-rolled microfluidic electrode array applied for vagus nerve stimulation in a rabbit model. Reprinted with permission from ref. 111. Copyright 2024, American Chemical Society. (d) Scanning electron microscopy (SEM) image showing high-resolution phototransistor arrays integrated with 3D liquid metal microelectrodes. (e) SEM image of 3D liquid metal electrode with Pt nanoclusters. Reprinted with permission from ref. 65. Copyright 2024, Springer Nature. (f) Optical microscopy image of a 3D liquid metal microelectrode array with varied pillar heights. (g) Optical microscopy image showing a retinal organoid positioned on a 3D liquid metal microelectrode array. Reprinted with permission from ref. 40. Copyright 2024, John Wiley and Sons. (h) Optical microscopy images of a magnetically reshapable 3D liquid metal electrode. Reprinted with permission from ref. 35. Copyright 2025, Springer Nature.

functional peripheral nerve interfaces. Moreover, Dong *et al.* proposed stretchable, self-rolled microfluidic electrode arrays fabricated *via* high-resolution (~30 μm) microfluidic printing of EGaIn ink, exhibiting high stretchability (~600% strain) and excellent biocompatibility (>8 weeks).[111] These electrodes transform into three-dimensional cuff-like structures that tightly wrap peripheral nerves, thereby enabling conformable neural interfaces for the vagus and sciatic nerves, as well as stable neural recording and effective neuromodulation (Fig. 7c).

3.4.2. Pillar structure. Furthermore, the most important feature enabling 3D structuring of liquid metals is the spontaneously formed surface oxide layer, which stabilizes otherwise unfavorable geometries despite the intrinsically high surface tension of bare liquid metal.[112] This thin oxide layer, with a thickness of approximately 1 to 5 nm, acts as a mechanically supportive shell that prevents the metal from collapsing, thereby allowing direct printing of 3D liquid-metal electrode architectures.[113–115] Leveraging this stabilization mechanism, recent studies have demonstrated diverse vertically standing pillar-type 3D microelectrodes for high-performance bioelectronic interfaces.[112,116–120]

For example, Chung *et al.* proposed a direct ink printing strategy in which gallium-based liquid metal was extruded vertically to form high-aspect-ratio liquid metal pillars (Fig. 7d), while the spontaneously formed oxide layer provided sufficient mechanical rigidity to maintain their 3D geometry during printing.[65] This oxide-assisted stabilization enabled the fabrication of freestanding liquid metal pillars on ultrathin

polymer substrates without collapse or spreading, which is not accessible with bare liquid metal in the absence of surface oxidation. As mentioned in Section 2.1.1, to enhance electrochemical performance, the authors electroplated platinum nanoclusters (Pt-black coating) onto the pillar surfaces, substantially reducing impedance while retaining the intrinsic softness and deformability of the liquid metal core (Fig. 7e). This combination of oxide-stabilized liquid metal printing and surface nanostructuring demonstrated how liquid metal electrodes can achieve both high mechanical compliance and improved charge-transfer efficiency.

In addition, Lee *et al.* introduced a parameter-controlled direct printing strategy, adjusting extrusion speed, dwell time, and nozzle-substrate distance to modulate the height and aspect ratio of printed liquid metal pillars[40] (Fig. 7f). This approach leveraged the interplay between liquid metal surface tension and the yield strength of the native oxide layer to reliably produce tall, slender, and mechanically compliant 3D structures. Because the printed pillars retain a low elastic modulus and high conformability, they maintain stable contact even with soft, deformable biological constructs such as retinal organoids without introducing significant mechanical stress. By tuning printing parameters, the authors created multi-height pillar arrays suitable for depth-resolved or volumetrically distributed interfaces within organoid tissues, demonstrating how oxide-stabilized liquid metal pillars can conform to and probe soft 3D biological environments (Fig. 7g). Kim *et al.* advanced the structural adaptability of liquid metal 3D electrodes by coating the sidewalls of printed pillars with a thin ferromagnetic cobalt layer.[35] In this design, direct printing again relied on oxide-mediated stabilization to create vertical pillars, but the addition of the magnetic shell endowed the pillars with mechanically reconfigurable behavior under external magnetic fields (Fig. 7h). This enabled non-destructive deflection, repositioning, and shape modulation of the electrodes, all while the liquid metal core preserved its electrical pathways and deformability. This study demonstrated how heterogeneous surface engineering, combining liquid metal fluidity, oxide-assisted rigidity, and magnetic actuation, can introduce new structural degrees of freedom that are difficult to realize with conventional solid electrodes.

4. Application

The materials and structures that have been discussed can be combined in various ways to produce synergistic effects. As a result, diverse types of 3D bioelectronic devices have been developed for a wide range of applications. This section discusses the representative device types and their corresponding functionalities.

4.1. Brain interfaces

4.1.1. Intracortical 3D neural interfaces. Surface interfaces inherently exhibit structural and functional limitations.[121] Most neurological disorders and cognitive functions arise not from superficial cortical layers alone, but from specific deep-brain structures (*e.g.*, hippocampus, basal ganglia, amygdala) or from interactions across multiple distributed neural networks.[122,123] Surface electrodes struggle to disentangle activity originating from different depths, capturing only aggregated signals projected onto the cortical surface. As a result, they are fundamentally constrained in resolving circuit-level neural dynamics, cell-type-specific population activity, and directed information flow between distinct brain regions.

To elucidate the pathophysiology of defined neural circuits or to deliver targeted stimulation to specific nuclei or neuronal populations for therapeutic purposes, three-dimensional penetrating electrode architectures that can be directly inserted into brain tissue are indispensable[81,124] (Fig. 8a and b). Accordingly, substantial technological progress has been made in advancing from surface-based electrode formats toward fully three-dimensional penetrating architectures. These 3D electrodes enable high-spatial-resolution recordings from deep and multi-layered structures, provide localized and precise electrical stimulation to targeted neuronal populations, and support comprehensive connectivity analyses through multi-channel, multi-dimensional configurations.

The primary advantage of 3D electrodes in brain interfacing lies in their ability to access and position recording sites within specific, predefined brain regions, enabling precise interrogation of deep and multilayered neural circuits.[81]

Although such architectures enable precise access to deep-brain structures, understanding complex neural computations requires not only depth access but also high-density, large-channel-count recording capabilities.[125–127] In line with this need, Liu *et al.* demonstrated a large-scale 3D microelectrode array capable of recording thousands of neurons across multiple cortical and subcortical regions simultaneously, providing a powerful example of how high-density architectures expand the spatial and functional coverage of intracortical interfaces[128] (Fig. 8c). Their device integrates vertically distributed electrode shanks within a 3D stacked configuration, enabling dense sampling across layers and regions without increasing the implantation footprint. Using this platform, the authors simultaneously mapped distributed neural ensembles in structures such as the PFC, motor cortex, and striatal pathways during behavior, revealing coordinated high-dimensional population dynamics that cannot be resolved using lower-density probes. Trautmann *et al.* further illustrated how high-density architectures enable comprehensive mapping of large-scale neural computations across multiple cortical areas[80] (Fig. 8d). Their work employed a multi-bank recording strategy, in which up to 384 channels could be densely allocated within a single bank or distributed across several banks spanning different depths and cortical regions. This flexible high-channel configuration allowed simultaneous recordings from distributed areas—including visual cortex, motor cortex, LIP, and inferotemporal cortex—within the same animal, capturing population-level dynamics underlying perception, motor planning, and decision-making. By leveraging thousands of recording sites across multiple banks, the study demonstrated that

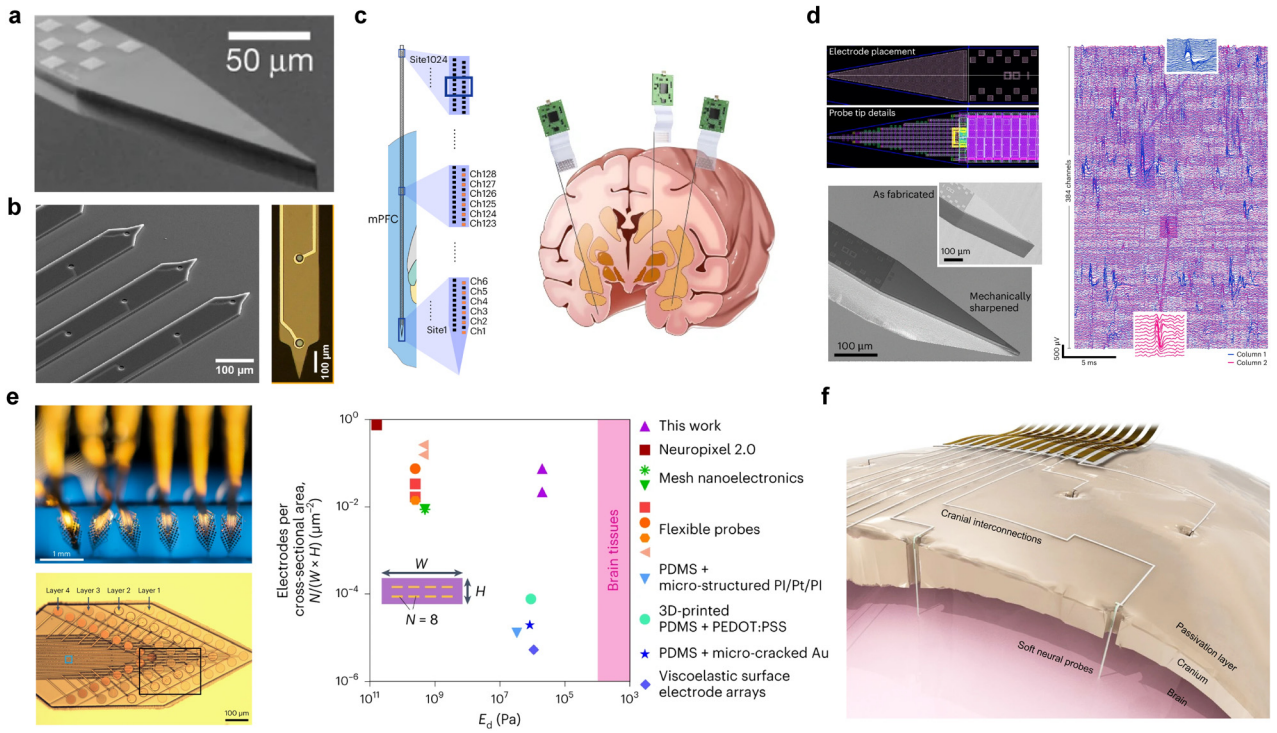

Fig. 8 Brain interfaces. (a) Scanning electron micrograph of the tip of a 3D silicon neural probe. Scale bar: 50 μm. Reprinted with permission from ref. 81. Copyright 2017, Springer Nature. (b) High-magnification SEM view of the flexible intracortical probes (left), and an optical close-up of a single shank tip (right). Scale bars: 100 μm. Reprinted with permission from ref. 124. Copyright 2021, Springer Nature. (c) Schematics illustrating the implantation of 10-mm Neuroscroll probes in the rat mPFC (left), and depicting brain-wide neural recordings in primates using Neuroscroll probes (right). Reprinted with permission from ref. 128. Copyright 2024, Springer Nature. (d) Close-up and SEM depiction of a shank tip that has been mechanically tilted to 25° out of plane (left), and raw multi-channel recordings (n = 384) from the motor cortex of a rhesus macaque (right). Reprinted with permission from ref. 80. Copyright 2025, Springer Nature. (e) A perfluoropolyether-based neural probe with four stacked electrode-array layers conformally wrapping a glass capillary (left), and a comparison of electrode count per cross-sectional area *versus* elastic modulus for cutting-edge neural probes (right). Reprinted with permission from ref. 8. Copyright 2023, Springer Nature. (f) Schematic illustration of liquid metal printing-based neural interface systems including direct cranial liquid metal printing and liquid metal neural probes. Reprinted with permission from ref. 132. Copyright 2024, Springer Nature.

high-density intracortical interfaces are essential for resolving coordinated neural activity patterns that emerge only at the scale of broad, interconnected neural networks.

Despite the advantages of 3D penetrating electrodes in achieving precise targeting and high-density recordings, their chronic performance remains fundamentally constrained by the mechanical mismatch between conventional probe materials and the extremely soft, viscoelastic nature of brain tissue.[129] Rigid or semi-rigid intracortical probes can induce micromotion-driven tissue damage, glial scarring, and long-term signal degradation, making the minimization of invasiveness a critical design requirement.[130,131] A central aspect of this challenge is the elastic modulus: while brain tissue exhibits moduli in the range of hundreds of pascals to a few kilopascals, most high-density electrode architectures rely on plastics or silicon-based dielectrics with moduli in the gigapascal range, producing large mechanical disparities at the tissue–device interface.[90,130] Accordingly, significant efforts have focused on engineering ultrasoft probe materials that reduce mechanical strain, mitigate chronic immune responses, and stabilize long-term neural recordings. For example, Le Floch *et al.* introduced a spatiotemporally scalable 3D soft neural probe platform built upon fluorinated elastomers with tissue-level mechanical softness (elastic modulus ≈0.5 MPa), yet capable of supporting multilayer, high-density electrode stacking without compromising flexibility or dielectric integrity[8] (Fig. 8e). Their perfluoropolyether-based dielectric elastomer remains chemically stable for months in physiological environments and enables nanometer-scale metal interconnects to be vertically integrated within a multilayer 3D configuration, achieving an unprecedented electrode density of 7.6 electrodes per 100 μm^2 while preserving exceptional compliance with brain tissue. This softness substantially suppresses chronic immune responses and reduces glial encapsulation compared with conventional plastic-based probes. Importantly, this approach occupies a design regime that has traditionally been difficult to achieve—combining brain-like mechanical softness with electrode densities comparable to or exceeding those of much stiffer silicon- or polymer-based probes—highlighting how material-level innovations are becoming essential to reconcile the competing demands of high-density architecture and long-term biocompatibility in next-generation 3D penetrating neural interfaces. On the other hand, Park *et al.* introduced an ultra-soft liquid-metal penetrating electrode platform designed to further

minimize implantation-induced and chronic brain damage using conductors whose mechanical properties approach those of neural tissue[132] (Fig. 8f). Their parylene-encapsulated eutectic gallium–indium (EGaIn) electrodes exhibit elastic moduli of ~330 kPa (Parylene/EGaIn) and ~233 kPa (Pt-black-coated EGaIn), which are four to six orders of magnitude softer than conventional metallic or silicon-based conductors ($E \approx 2.6 \times 10^6$ kPa). This dramatic reduction in stiffness enables the electrodes to deform with brain micromotions rather than cutting through tissue, thereby reducing shear stress, suppressing inflammatory responses, and minimizing long-term glial encapsulation. Moreover, the intrinsic flowability and self-healing nature of the liquid metal ensure electrical continuity even under large strains. A distinguishing feature of this work is the ability to form not only intracortical liquid-metal pathways but also conformal circuit patterns on the skull surface through the same material system, establishing a hybrid intracortical–epicranial interface without additional rigid components.

Together, these advances highlight a clear trajectory in the evolution of brain-interfacing technologies: from rigid, low-channel devices toward soft, high-density, and structurally adaptable 3D architectures that more faithfully match the mechanical and organizational complexity of neural tissue. As the field continues to integrate material innovations with scalable fabrication and multimodal functionality, next-generation neural interfaces are increasingly poised to achieve long-term stability, reduced invasiveness, and comprehensive access to the brain's multiscale computational processes—ultimately bridging the gap between biological neural circuits and engineered electronic systems.

4.1.2. Challenges. Despite these various studies, several important challenges still remain for intracortical three-dimensional neural interfaces, particularly in terms of long-term deployment and scalability.[133] In particular, probes fabricated from ultrasoft materials can improve mechanical compliance with brain tissue, but they also present significant challenges for insertion into deep brain regions. Therefore, balancing tissue-level mechanical compliance with sufficient stiffness for reliable insertion remains a critical design consideration.[134] These limitations have led to the development of auxiliary insertion strategies, such as insertion shuttles, biodegradable coatings, and syringe-based delivery methods; however, these approaches may increase surgical complexity and introduce additional risks of tissue damage.[135] In addition, as intracortical interfaces evolve toward high-channel-count and high-density architectures, the complexity of interconnects, wiring, packaging, and overall system integration increases substantially. This challenge extends beyond simply increasing the number of electrodes, as device footprint, mechanical stiffness, electrical reliability, and long-term system stability must all be optimized simultaneously.[136] Therefore, next-generation intracortical 3D neural interfaces must achieve not only high recording density and precise neural access, but also reliable insertion, scalable channel integration, robust packaging, and system-level reliability for long-term operation.

4.2. Retinal interface

Retinal interface technologies have gained increasing attention in response to the growing population affected by visual impairment. Vision is generated as incident light is detected by photoreceptor cells, transmitted to retinal ganglion cells (RGCs), and subsequently conveyed to the brain *via* the optic nerve. In retinal degenerative diseases, photoreceptors progressively degenerate, ultimately leading to blindness. However, neurons in the inner retinal layers, including RGCs, remain comparatively undamaged,[137,138] which has motivated the development of retinal prostheses designed to electrically stimulate these surviving neurons to restore visual perception.

Conventional retinal prostheses have predominantly adopted planar architectures; however, their limited conformability to the curved retinal surface hinders precise targeting of retinal neurons and necessitates higher charge injection, often resulting in electrical crosstalk. In contrast, 3D architectures can be implanted conformally onto retinal tissue, enabling intimate electrode-cell contact, improved targeting, and reduced stimulation thresholds.

Two principal modalities of retinal prostheses, retinal and epiretinal, share the overarching objective of stimulating residual retinal neurons, yet differ substantially in anatomical placement and functional characteristics. Subretinal prostheses are positioned between the photoreceptor layer and the retinal pigment epithelium (RPE), whereas epiretinal prostheses are implanted between the sclera and the choroid.[65]

4.2.1. Subretinal prosthesis. Subretinal prostheses aim to minimize the distance between stimulation electrodes and degenerated photoreceptors, thereby promoting more physiologically natural vision restoration. Leveraging this anatomical advantage, Mathieson *et al.* developed a photovoltaic subretinal implant composed of 25 μm pixels incorporating three photodiodes per pixel.[84] Owing to its photovoltaic architecture, the device receives both power and data *via* pulsed near-infrared (NIR) illumination. *Ex vivo* stimulation of degenerate rat retinas elicited robust neuronal spiking, demonstrating that high-density photovoltaic arrays can effectively activate retinal circuits.

Subsequent *in vivo* experiments by Mandel *et al.* confirmed that the implanted device produced electrically evoked visual potentials (eVEPs) similar in shape to natural visually evoked potentials (VEPs).[139] Notably, eVEP amplitude exhibited modulation by pulse duration, frequency, and intensity, suggesting that the device can emulate dynamic features of natural visual processing. Representative pixel architecture is shown in Fig. 9a. Clinical studies further demonstrated both safety[140] and simultaneous use of prosthetic vision and natural vision[141] in patients with age-related macular degeneration (AMD), achieving visual acuities ranging from 20/438 to 20/550 (Fig. 9b).

Despite these advances, achieving clinically meaningful acuity (20/200 or better) requires pixel sizes below 50 μm, which had not been achieved.[142] Ho *et al.* compared flat and pillar electrode arrays to address this limitation. Although a 55 μm flat pixel array achieved 20/192 acuity, further reduction to 40 μm resulted in increased stimulation thresholds and

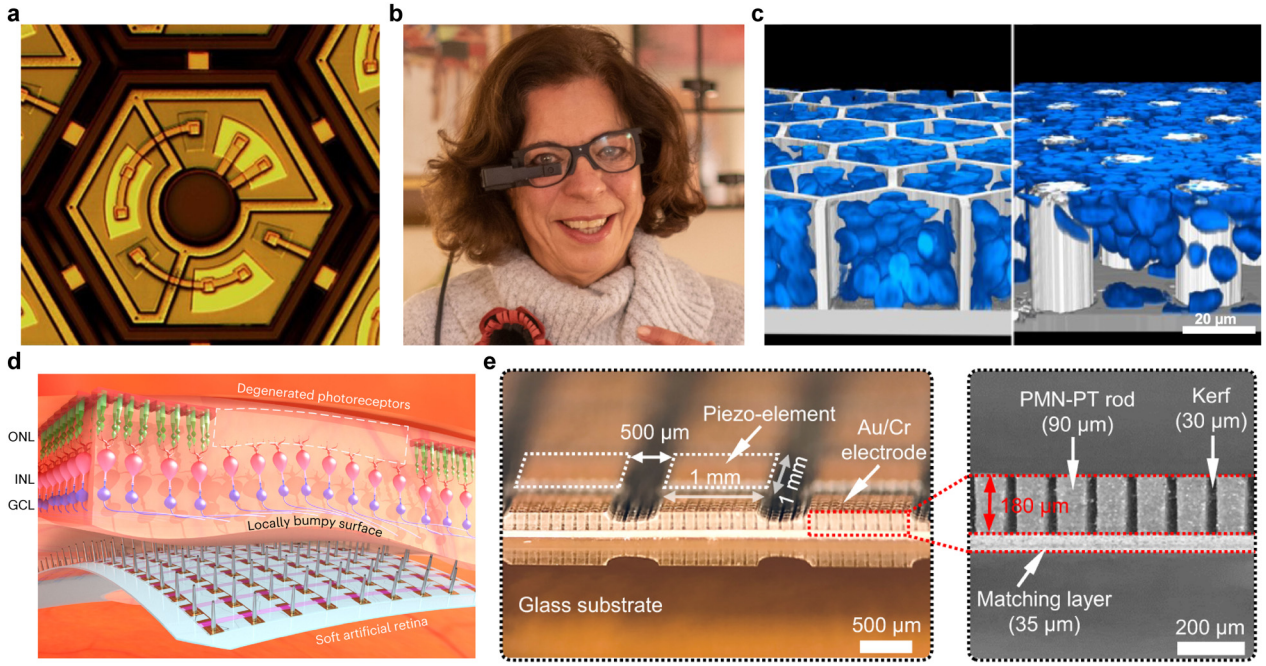

Fig. 9 Retinal interfaces. (a) Microscopy showing the 140 μm pixel architecture of a photovoltaic subretinal prosthesis device. Reprinted with permission from ref. 139. Copyright 2013, Springer Nature. (b) Photograph of a participant of the retinal prosthetic device clinical trial. Reproduced from ref. 141, *via* Creative Commons CC BY 4.0 International license. Copyright 2022, Springer Nature. (c) Simulation demonstrating the adhesion of retinal cells to the honeycomb and pillar structured prostheses. Scale bar, 20 μm. Reprinted with permission from ref. 85. Copyright 2025, Springer Nature. (d) Schematic of the subretinal prosthesis with 3D liquid metal pillars in proximity to the locally bumpy retinal surface. Reprinted with permission from ref. 65. Copyright 2024, Springer Nature. (e) (left) Photograph showing the 3D composite with an Au/Cr electrode and a piezo element. Scale bar, 500 μm. (right) Cross-section of the composite. Scale bar, 200 μm. Reprinted with permission from ref. 146. Copyright 2022, Springer Nature.

diminished VEP amplitude and SNR. Pillar electrodes (10 μm height) provided closer proximity to target neurons but were constrained by spherical expansion of electric fields, limiting feasible reductions in pixel size.

To further decouple pixel size from visual acuity constraints, Flores *et al.* introduced a 3D honeycomb architecture consisting of vertical walls (25 μm height) surrounding each pixel, with active electrodes at the base and return electrodes on the upper wall surfaces.[143] This configuration aligned electric fields with the orientation of bipolar cells, reducing stimulation thresholds. Confocal imaging six weeks post-implantation showed that retinal cells consistently migrated into wells of 20, 30, and 40 μm arrays, maintaining intimate electrode–cell contact.

Bhuckory *et al.* evaluated planar, honeycomb, and pillar electrode geometries and reported that planar arrays enabled safer device removal, whereas honeycomb structures exhibited stronger adhesion to the retina, and pillar electrodes tended to attach to retinal tissue.[85] Nevertheless, for maximizing potential visual acuity, honeycomb and pillar designs outperformed planar configurations due to their extensive contact with the inner nuclear layer (Fig. 9c). The honeycomb architecture was especially promising because its electric-field alignment effectively decoupled pixel size and stimulation threshold, which is an advantage not observed in pillar designs.

Beyond these geometries, Bendali *et al.* developed a well-structured 3D array incorporating boron-doped diamond electrodes.[144] Confocal images revealed substantial cellular migration into the wells, which concentrated current flow within individual wells and substantially reduced crosstalk, as confirmed by current–density measurements.

4.2.2. Epiretinal prosthesis. Epiretinal prostheses are positioned on the inner surface of the retina, enabling surgical access through comparatively safer procedures. Watanabe *et al.* introduced an epiretinal system utilizing vertically stacked large-scale integration (LSI) chips integrating photodetectors, image-processing units, and stimulation circuits.[145] The minimized interconnect length contributed to compact device dimensions and rapid signal processing. *In vivo* rabbit experiments successfully recorded electrically evoked potentials (EEP), demonstrating functional retinal stimulation.

Chung *et al.* addressed limitations associated with rigid prostheses, such as unintended axonal stimulation and retinal damage, by fabricating a soft pillar array using a eutectic gallium–indium alloy.[65] The directly printed soft pillars enhanced biocompatibility and targeting accuracy (Fig. 9d). *Ex vivo* mouse retina experiments showed RGC spiking upon stimulation, while *in vivo* tests on retinal-degenerated mice demonstrated consistent electrical responses under visible light illumination. Localized laser exposure through a photomask produced spatially selective retinal activation, confirming precise stimulation capabilities.

An alternative strategy using ultrasound as the stimulation medium was reported by Jiang *et al.*, who developed a piezoelectric electrode array capable of converting incident ultrasound into alternating current (AC), which was then rectified to

direct current (DC) for neural activation[146] (Fig. 9e). This device could generate artificial visual patterns such as "S", "H", and "V". The *ex vivo* calcium imaging confirmed selective neuronal activation in expected regions.

4.2.3. Challenges. Despite notable progress, several key challenges hinder the full clinical translation of retinal prostheses. First, while reduction of electrode size is desired for better resolution, such implementation typically increases impedance, thereby elevating stimulation thresholds.[147,148] Although electrodeposition of a platinum-black electrode coating has been proposed to lower impedance, such approaches may be challenging to apply to complex 3D geometries.[149] In addition, significant performance improvements are still required regarding pixel size–acuity relationships, image-processing strategies, reliable power, and data delivery systems.[150,151]

Nevertheless, the rapid evolution of device architectures, materials, and stimulation modalities continues to expand the capabilities of retinal prostheses. Sustained interdisciplinary innovation is expected to further address these limitations and guide the field toward clinically viable, high-resolution artificial vision.

4.3. Organoid interface

3D neural bioelectronics have significantly contributed to the advancement of next-generation healthcare technologies through the monitoring and stimulation of neural signals. However, challenges remain in clinical translation due to limited accessibility to internal organs and stringent regulatory requirements for implantable devices.[152] In this context, organoids, self-organized 3D structures derived from human stem cells, offer a novel *in vitro* interface that enables real-time access to physiologically relevant human signals, effectively replacing ethically and technically constrained *in vivo* models.[153] Organoids reliably mimic the structure, function, and disease pathophysiology of specific organs, such as the brain, retina, and heart. Their ability to be produced using patient-derived cells makes them advantageous for personalized treatment research that reflects individual genetic and pathological characteristics.[154] The integration of 3D bioelectronics with organoids provides new opportunities to access human-like bioelectrical signals in real-time without the ethical and technical limitations of *in vivo* models.[13]

4.3.1. Rigid 3D interfaces. To fully exploit the 3D structure of organoids, various multifunctional electrodes have been developed to 3D interface with their surfaces or interiors. Early approaches utilized rigid electrodes fabricated in 3D geometries that physically penetrate the organoid tissue. For example, Shin *et al.* developed a 3D high-density multifunctional MEA with integrated optical stimulation and drug delivery channels[155] (Fig. 10a). The device included 63 recording microelectrodes across 18 shanks, enabling neural activity monitoring and synaptic latency measurements in 3D neural networks. Optical fibers and microfluidic channels allowed for localized stimulation *via* light and chemicals. However, these rigid electrodes exhibit mechanical mismatch with the soft tissue of organoids due to their high Young's modulus, often leading to tissue damage and instability during long-term measurements.

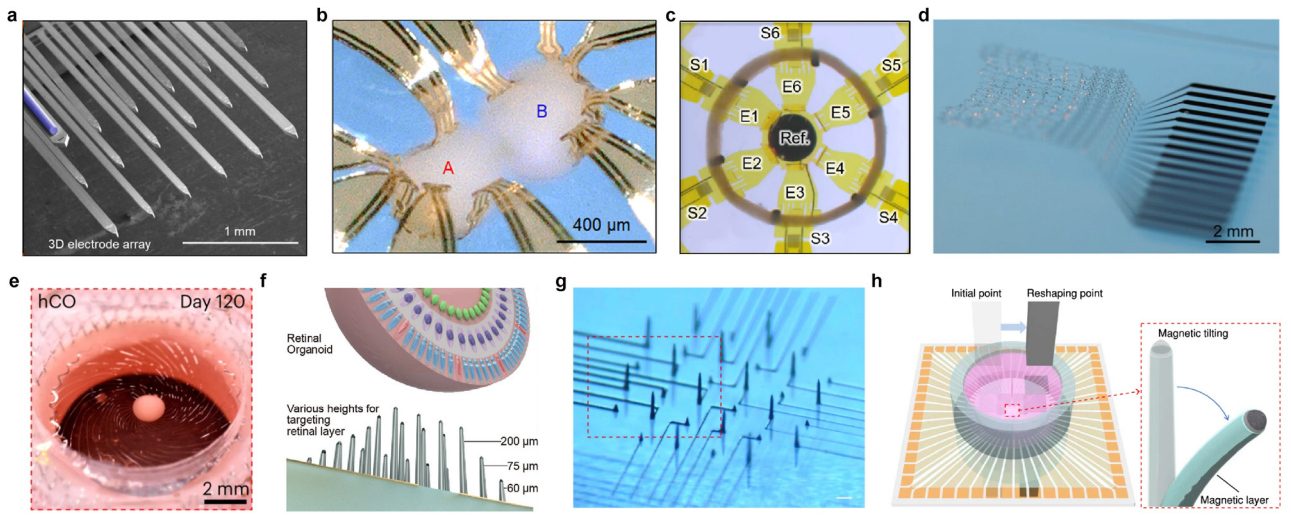

Fig. 10 Three-dimensional organoid interfaces. (a) Rigid 3D multifunctional microelectrode array. Reprinted with permission from ref. 155. Copyright 2021, Springer Nature. (b) A 3D multifunctional mesoscale scaffold that maintains stable contact and records neural activity from assembloids. Reprinted with permission from ref. 102. Copyright 2021, American Association for the Advancement of Science. (c) Engineered cardiac tissues integrated with the same 3D multifunctional mesoscale scaffold. Reprinted with permission from ref. 157. Copyright 2024, American Association for the Advancement of Science. (d) Stretchable mesh nanoelectronics released from the substrate and freely suspended in saline solution. Reprinted with permission from ref. 72. Copyright 2022, John Wiley and Sons. (e) Photographs of a spiral kirigami-electronics (KiriE) assembly coupled with human cortical organoids (hCO). Reprinted with permission from ref. 158. Copyright 2024, Springer Nature. (f) 3D liquid-metal (LM) multielectrode array with various heights for retinal organoids. Reprinted with permission from ref. 40. Copyright 2024, John Wiley and Sons. (g) Optical micrographs of LM interconnects and 3D LM pillars with variable heights. (h) Schematic illustration of a magnetically reshapable 3D LM microelectrode array (MEA). Reprinted with permission from ref. 35. Copyright 2025, Springer Nature.

4.3.2. Flexible surface-conformal interfaces. Recent advances in flexible and biocompatible electronics have enabled the development of 3D electrode systems that can interface intimately with organoids. These electrodes are designed to gently conform to the complex 3D geometry of organoids, thereby supporting stable, long-term, and non-invasive recording of bioelectrical signals. Planar 2D electrodes were transformed into shell-like 3D devices conforming to organoid surfaces through self-folding mechanisms. Cools *et al.* introduced a dynamic MEA platform utilizing residual stress-induced self-folding, resulting in individually addressable electrodes that form shell-like structures.[156] These shell-like 3D devices wrap around organoids and enable spatiotemporal mapping of action potentials, demonstrated in cultured neonatal rat ventricular cardiomyocytes. Similarly, the Rogers group developed compliant, 3D multifunctional mesoscale frameworks (3D MMF) for interfacing with spheroids and assembloids. These platforms support multimodal sensing and stimulation, including electrical, optical, chemical, and thermal modalities[102] (Fig. 10b). The system supports high-resolution, multichannel electrical recordings across the entire curved surface of cortical spheroids, allowing for precise mapping of spontaneous neural activity. Synchronized bursting observed across multiple electrode channels enabled quantification of functional connectivity within the spheroid. Moreover, when two spheroids were fused to form an assembloid, the 3D MMF enabled real-time electrical monitoring of bridging tissue formation and growth, providing dynamic observation of inter-spheroid network reconstruction. The platform was also used in engineered cardiac tissues for real-time, simultaneous monitoring of electrophysiological and mechanical activity[157] (Fig. 10c). Pharmacological interventions with agents such as isoproterenol and sotalol induced dose-dependent alterations in beating rate, contractile force, and QT intervals, demonstrating the platform's capacity for multiparametric drug response profiling. These findings highlight the potential of these 3D electrode systems for cardiac disease modeling and therapeutic screening.

4.3.3. Stretchable mesh interfaces. In addition, an ultrathin and highly flexible mesh electrode was developed to minimize the mechanical mismatch with organoid tissue, allowing the device to naturally integrate into the tissue and form stable contacts for long-term electrophysiological recordings. Floch *et al.* designed a mesh electrode with a highly flexible and stretchable structure that matches the mechanical properties of brain organoids[72] (Fig. 10d). The device was also engineered to fold through organogenesis driven by neural progenitors or stem cells, enabling the distribution of stretchable electrode arrays throughout the entire 3D organoid structure, forming a ''cyborg brain organoid'' platform. The authors successfully recorded single-cell electrophysiological signals within 3D cultured tissues continuously for up to 10 months, which allowed precise tracking of cellular activity dynamics and network formation over time. Yang *et al.* introduced kirigami electronics (KiriE) that transform from planar precursors into 3D spiral or honeycomb geometries to stably interface with neural organoids in suspension[158] (Fig. 10e). These devices enabled chronic single-unit electrophysiological recordings from intact cortical organoids for up to 120 days while preserving their morphology, cytoarchitecture, and cell composition throughout development. KiriE further supported optogenetic and pharmacological perturbations, reliably capturing light-evoked responses and drug-induced changes in firing rates. Overall, the kirigami-based architecture provides a conformal, minimally invasive interface for long-term probing of neural development and circuit-level phenotypes in 3D organoid systems.

4.3.4. Soft and reconfigurable interfaces. With advances in soft materials, devices capable of long-term, stable interfacing with internal organoid regions were developed. Lee *et al.* fabricated a 3D MEA using soft liquid metal *via* direct high-resolution 3D printing for electrophysiological recordings in retinal organoids[40] (Fig. 10f). The use of LM enabled precise targeting of specific inner retinal layers within the 3D structure of retinal organoids. In addition, the liquid metal-based 3D MEAs exhibited high mechanical compliance and adaptability to the complex geometry of organoids, facilitating stable internal recordings without causing tissue damage. Kim *et al.* engineered magnetically responsive 3D LM microelectrode pillars by coating one side of each pillar with a thin ferromagnetic cobalt layer, enabling shape reconfiguration in response to externally applied magnetic fields[35] (Fig. 10g). This magnetic actuation allowed controlled bending and repositioning of individual electrodes without mechanical fracture, leveraging the intrinsic softness of EGaIn. Considering the typical size of neuronal cell bodies, about 12 μm, the electrically active tip of the electrode needed to travel at least 24 μm to contact a different group of neurons for signal recording. In experiments applying bidirectional magnetic gradients to a single movable electrode, the maximum tilt angle of the 3D liquid metal pillar was measured as $51.6 \pm 0.21^{\circ}$, corresponding to a tip displacement of 234 μm, which is sufficient to reach other neurons (Fig. 10h). Using this soft and reconfigurable interface, they obtained high-fidelity recordings of diverse neural activities, including spikes and burst dynamics, from spatially distinct regions without inducing structural damage to the tissue. Collectively, the study presents a mechanically adaptive bioelectronic interface that circumvents the spatial rigidity of conventional fixed electrodes in 3D neural systems.

4.3.5. Challenges. Despite these significant advances, several challenges remain in establishing reliable bioelectronic interfaces for organoid recordings. First, the inherently spherical geometry of organoids presents difficulties in achieving comprehensive volumetric mapping of neural activity across the entire structure, and realizing high-density recordings with full 3D coverage remains an important goal. Second, variability in organoid size and morphology poses challenges for standardization and reproducibility across experiments.[35] In addition, as organoids undergo continuous growth and maturation, electrodes in contact with the tissue can shift or lose stable contact, thereby compromising the reliability of long-term signal recordings.[159] Nevertheless, continued advances in soft bioelectronics and adaptive interface designs are expected to

Table 1 Mechanical and electrochemical properties of different 3D neural electrode architectures

Material	3D architecture	Electrode diameter	Impedance at 1 kHz	Charge storage capacity	Elastic modulus	Bending stiffness	Ref.
Metal	Soft mesh electronics	25 μm	140 ± 50 kΩ	Not specified	300 kPa	Not specified	66
	Serpentine electronics	15 μm	Not specified		~25 MPa		69
Silicon	Shank-type electronics	12 μm	150 kΩ	Not specified	~170 GPa	Not specified	80
	Array-type electronics	2–3 μm	100–300 kΩ		~170 GPa		83
Polymer	Cuff structure	100 μm	4.1 ± 0.4 kΩ	Not specified	1.24 GPa	21 Pa mm^3	96
	Kirigami structure	15 μm	39.1 ± 3.4 kΩ		1.7 GPa	7.1 N $μm^3$	99
	Pillar structure	8 μm	35.2 kΩ		4.73 GPa	3.86 N $μm^3$	100
	Wrapping structure	30 μm	327.7 kΩ		Not specified	Not specified	103
	Microneedle structure	10–30 μm	1.6 kΩ		6.6 GPa	Not specified	104
Liquid metal	Pillar structure	8 μm	506.93 kΩ	Not specified	204 kPa	1.05×10^{-11} N m	40
	Pillar structure with Pt-black nanoclusters	4 μm	210 kΩ	72.84 mC cm^{-2}	234 kPa	Not specified	65

further improve the stability and spatial coverage of organoid-electrode platforms in the future.

Conclusions

Neural interfaces have undergone rapid development alongside the growing interest in neural signal acquisition and modulation. Despite significant progress toward scalable, biocompatible and stable sensors, several critical challenges remain unresolved. Conventional 2D neural interfaces have been extensively studied,[160,161] but their inherent limitations, particularly in conformability to complex biological tissues, restrict their long-term performance and applicability.

To address these limitations, a wide range of 3D neural interfaces have been introduced. By leveraging diverse materials, architectures and fabrication strategies, these 3D systems have demonstrated enhanced tissue integration, high spatial uniformity, and improved signal resolution. These advancements are reflected in the various performance metrics of the devices introduced throughout this review (Table 1). Such advances have expanded the scope of neural interfacing beyond the brain to include the retina, peripheral organs, and even *in vitro* models such as organoids.

Nevertheless, the invasive nature of 3D electrodes continues to pose substantial challenges, including foreign body responses and chronic inflammation. Ongoing efforts to mitigate these issues have been made, such as the development of soft, adaptive, and biodegradable materials. These suggest promising directions toward improving long-term compatibility and functionality. Continued interdisciplinary research integrating materials science, bioengineering, and neuroscience will further advance 3D neural interfaces and ultimately enable transformative breakthroughs in neural recording and stimulation technologies.

Author contributions

J. P., W. P., H. S., I. J., M. O., E. K., D. K., S. H. A., Y. K., W. G. C., S. L., and J. L. wrote the manuscript. J. P., W. P., H. S., I. J., M. O., E. K., D. K., S. H. A., Y. K., W. G. C., S. L., and J. L. further revised the manuscript. J. A. L. and J.-U. P. supervised, reviewed, and edited the manuscript.

Conflicts of interest

There are no conflicts of interest to declare.

Data availability

No primary research results, code or software have been included and no new data were generated or analyzed as part of this review.

Acknowledgements

This work was supported by the Ministry of Science & ICT (MSIT), the Ministry of Trade, Industry and Energy (MOTIE), the Ministry of Health & Welfare, and the Ministry of Food and Drug Safety of Korea through the National Research Foundation (RS-2023-NR077138, RS-2025-16063568, RS-2025-18362970, RS-2024-00464032, and RS-2025-00514998), the STEAM Research Program (RS-2024-00460364), ERC Program (RS-2024-00406240), and the Technology Innovation Program (RS-2025-08672969). This work was also funded by the Korea Institute of Science and Technology (KIST) Institutional Program (2E33191 and 2E33190) and the Institute for Basic Science (IBS-R026-D1).

Notes and references

1 W. Park, H. Seo, J. Kim, Y.-M. Hong, H. Song, B. J. Joo, S. Kim, E. Kim, C.-G. Yae, J. Kim, J. Jin, J. Kim, Y. Lee, J. Kim, H. K. Kim and J.-U. Park, *Nat. Commun.*, 2024, **15**, 2828.
2 H. Song, H. Shin, H. Seo, W. Park, B. J. Joo, J. Kim, J. Kim, H. K. Kim, J. Kim and J.-U. Park, *Adv. Sci.*, 2022, **9**, 2203597.
3 M. Ku, J. Kim, J.-E. Won, W. Kang, Y.-G. Park, J. Park, J.-H. Lee, J. Cheon, H. H. Lee and J.-U. Park, *Sci. Adv.*, 2020, **6**, eabb2891.
4 F. Tehrani, H. Teymourian, B. Wuerstle, J. Kavner, R. Patel, A. Furmidge, R. Aghavali, H. Hosseini-Toudeshki, C. Brown, F. Zhang, K. Mahato, Z. Li, A. Barfidokht, L. Yin,

P. Warren, N. Huang, Z. Patel, P. P. Mercier and J. Wang, *Nat. Biomed. Eng.*, 2022, **6**, 1214–1224.
5 R. A. Ajjan, M. H. Cummings, P. Jennings, L. Leelarathna, G. Rayman and E. G. Wilmot, *Diabetes Vasc. Dis. Res.*, 2018, **15**, 175–184.
6 S. Lee, W. G. Chung, E. Kim, E. Kim, J. Paek, D. Kim, S. H. An, T. Lee, J. A. Lim and J.-U. Park, *Lab Chip*, 2025, **25**, 4508–4541.
7 M. Kim, S. Kim, Y. W. Kwon, H. Seo, W. G. Chung, E. Kim, W. Park, H. Song, D. H. Lee, J. Lee, S. Lee, I. Jeong, K. Lim, D.-Y. Jo and J.-U. Park, *Adv. Sens. Res.*, 2023, **2**, 2200049.
8 P. Le Floch, S. Zhao, R. Liu, N. Molinari, E. Medina, H. Shen, Z. Wang, J. Kim, H. Sheng, S. Partarrieu, W. Wang, C. Sessler, G. Zhang, H. Park, X. Gong, A. Spencer, J. Lee, T. Ye, X. Tang, X. Wang, K. Bertoldi, N. Lu, B. Kozinsky, Z. Suo and J. Liu, *Nat. Nanotechnol.*, 2024, **19**, 319–329.
9 S. M. Yun, M. Kim, Y. W. Kwon, H. Kim, M. J. Kim, Y.-G. Park and J.-U. Park, *Appl. Sci.*, 2021, **11**, 1235.
10 J. Kim, E. Cha and J.-U. Park, *Adv. Mater. Technol.*, 2020, **5**, 1900728.
11 I. Jeong, W. G. Chung, E. Kim, W. Park, H. Song, J. Lee, M. Oh, E. Kim, J. Paek, T. Lee, D. Kim, S. H. An, S. Kim, H. Cho and J.-U. Park, *Mater. Horiz.*, 2025, **12**, 6587–6621.
12 M. Oh, E. Kim, J. Lee, I. Jeong, E. Kim, J. Paek, T. Lee, D. Kim, S. H. An, S. Kim, J. A. Lim and J.-U. Park, *Adv. Sens. Res.*, 2025, **4**, e00028.
13 W. G. Chung, E. Kim, H. Song, J. Lee, S. Lee, K. Lim, I. Jeong and J.-U. Park, *Adv. NanoBiomed Res.*, 2022, **2**, 2200081.
14 S. Kim, Y. W. Kwon, H. Seo, W. G. Chung, E. Kim, W. Park, H. Song, D. H. Lee, J. Lee, S. Lee, K. Lim, I. Jeong, D.-Y. Jo and J.-U. Park, *ACS Appl. Electron. Mater.*, 2023, **5**, 1926–1946.
15 E. Kim, S. Kim, Y. W. Kwon, H. Seo, M. Kim, W. G. Chung, W. Park, H. Song, D. H. Lee, J. Lee, S. Lee, I. Jeong, K. Lim and J.-U. Park, *Interdiscip. Med.*, 2023, **1**, e20230003.
16 S. Min, S. Kim, W.-S. Sim, Y. S. Choi, H. Joo, J.-H. Park, S.-J. Lee, H. Kim, M. J. Lee, I. Jeong, B. Cui, S.-H. Jo, J.-J. Kim, S. B. Hong, Y.-J. Choi, K. Ban, Y.-G. Kim, J.-U. Park, H.-A. Lee, H.-J. Park and S.-W. Cho, *Nat. Commun.*, 2024, **15**, 2564.
17 H. Song, M. Kim, E. Kim, J. Lee, I. Jeong, K. Lim, S. Y. Ryu, M. Oh, Y. Kim and J.-U. Park, *BMEMat*, 2024, **2**, e12048.
18 H. Seo, W. G. Chung, Y. W. Kwon, S. Kim, Y.-M. Hong, W. Park, E. Kim, J. Lee, S. Lee, M. Kim, K. Lim, I. Jeong, H. Song and J.-U. Park, *Chem. Rev.*, 2023, **123**, 11488–11558.
19 Y. Luo, M. R. Abidian, J.-H. Ahn, D. Akinwande, A. M. Andrews, M. Antonietti, Z. Bao, M. Berggren, C. A. Berkey, C. J. Bettinger, J. Chen, P. Chen, W. Cheng, X. Cheng, S.-J. Choi, A. Chortos, C. Dagdeviren, R. H. Dauskardt, C. Di, M. D. Dickey, X. Duan, A. Facchetti, Z. Fan, Y. Fang, J. Feng, X. Feng, H. Gao, W. Gao, X. Gong, C. F. Guo, X. Guo, M. C. Hartel, Z. He, J. S. Ho, Y. Hu, Q. Huang, Y. Huang, F. Huo, M. M. Hussain, A. Javey, U. Jeong, C. Jiang, X. Jiang, J. Kang, D. Karnaushenko, A. Khademhosseini, D.-H. Kim, I.-D. Kim, D. Kireev, L. Kong, C. Lee, N.-E. Lee, P. S. Lee, T.-W. Lee, F. Li, J. Li, C. Liang, C. T. Lim, Y. Lin, D. J. Lipomi, J. Liu, K. Liu, N. Liu, R. Liu, Y. Liu, Y. Liu, Z. Liu, Z. Liu, X. J. Loh, N. Lu, Z. Lv, S. Magdassi, G. G. Malliaras, N. Matsuhisa, A. Nathan, S. Niu, J. Pan, C. Pang, Q. Pei, H. Peng, D. Qi, H. Ren, J. A. Rogers, A. Rowe, O. G. Schmidt, T. Sekitani, D.-G. Seo, G. Shen, X. Sheng, Q. Shi, T. Someya, Y. Song, E. Stavrinidou, M. Su, X. Sun, K. Takei, X.-M. Tao, B. C. K. Tee, A. V.-Y. Thean, T. Q. Trung, C. Wan, H. Wang, J. Wang, M. Wang, S. Wang, T. Wang, Z. L. Wang, P. S. Weiss, H. Wen, S. Xu, T. Xu, H. Yan, X. Yan, H. Yang, L. Yang, S. Yang, L. Yin, C. Yu, G. Yu, J. Yu, S.-H. Yu, X. Yu, E. Zamburg, H. Zhang, X. Zhang, X. Zhang, X. Zhang, Y. Zhang, Y. Zhang, S. Zhao, X. Zhao, Y. Zheng, Y.-Q. Zheng, Z. Zheng, T. Zhou, B. Zhu, M. Zhu, R. Zhu, Y. Zhu, Y. Zhu, G. Zou and X. Chen, *ACS Nano*, 2023, **17**, 5211–5295.
20 H. Huh, H. Shin, H. Li, K. Hirota, C. Hoang, S. Thangavel, M. D'Alessandro, K. A. Feltman, L. Sentis and N. Lu, *Device*, 2025, **3**, 100781.
21 H. Shim, K. Sim, F. Ershad, P. Yang, A. Thukral, Z. Rao, H.-J. Kim, Y. Liu, X. Wang, G. Gu, L. Gao, X. Wang, Y. Chai and C. Yu, *Sci. Adv.*, 2019, **5**, eaax4961.
22 Y. W. Kwon, Y. S. Jun, Y.-G. Park, J. Jang and J.-U. Park, *Nano Res.*, 2021, **14**, 3070–3095.
23 J. Jang, H. Kim, Y. M. Song and J.-U. Park, *Opt. Mater. Express, OME*, 2019, **9**, 3878–3894.
24 Y. H. Cho, Y.-G. Park, S. Kim and J.-U. Park, *Adv. Mater.*, 2021, **33**, 2005805.
25 B. G. Hyun, H. J. Son, S. Ji, J. Jang, S.-H. Hur and J.-U. Park, *J. Electroceram.*, 2017, **38**, 43–50.
26 M.-S. Lee, J. Kim, J. Park and J.-U. Park, *Nanoscale Res. Lett.*, 2015, **10**, 27.
27 J. Paek, J. Kim, B. Wan An, J. Park, S. Ji, S.-Y. Kim, J. Jang, Y. Lee, Y.-G. Park, E. Cho, S. Jo, S. Ju, W. Hyung Cheong and J.-U. Park, *FlatChem*, 2017, **3**, 71–91.
28 K. Kim, B. G. Hyun, J. Jang, E. Cho, Y.-G. Park and J.-U. Park, *J. Inf. Disp.*, 2016, **17**, 131–141.
29 S. Ji, J. Jang, J. C. Hwang, Y. Lee, J.-H. Lee and J.-U. Park, *Adv. Mater. Technol.*, 2020, **5**, 1900928.
30 H. S. An, Y.-G. Park, K. Kim, Y. S. Nam, M. H. Song and J.-U. Park, *Adv. Sci.*, 2019, **6**, 1901603.
31 Y. Jo, J. Y. Kim, S.-Y. Kim, Y.-H. Seo, K.-S. Jang, S. Y. Lee, S. Jung, B.-H. Ryu, H.-S. Kim, J.-U. Park, Y. Choi and S. Jeong, *Nanoscale*, 2017, **9**, 5072–5084.
32 K. Lim, H. Seo, W. G. Chung, H. Song, M. Oh, S. Y. Ryu, Y. Kim and J.-U. Park, *Commun. Mater.*, 2024, **5**, 49.
33 M. Kim, E. J. Jeon, W. G. Chung, H. Kim, E. Kim, S. Lee, J.-H. Lee, S.-W. Cho and J.-U. Park, *Adv. Mater.*, 2025, **37**, 2419250.
34 S. Park, Y. J. Song, H. Boo and T. D. Chung, *J. Phys. Chem. C*, 2010, **114**, 8721–8726.
35 E. Kim, E. Jeong, Y.-M. Hong, I. Jeong, J. Kim, Y. W. Kwon, Y.-G. Park, J. Lee, S. Choi, J.-Y. Kim, J.-H. Lee, S.-W. Cho and J.-U. Park, *Nat. Commun.*, 2025, **16**, 2011.

36 S. F. Cogan, *Annu. Rev. Biomed. Eng.*, 2008, **10**, 275–309.
37 Y. W. Kwon, E. Kim, C. S. Koh, Y.-G. Park, Y.-M. Hong, S. Lee, J. Lee, T. J. Kim, W. Mun, S. H. Min, S. Kim, J. A. Lim, H. H. Jung and J.-U. Park, *ACS Nano*, 2025, **19**, 7337–7349.
38 D. Viana, S. T. Walston, E. Masvidal-Codina, X. Illa, B. Rodríguez-Meana, J. del Valle, A. Hayward, A. Dodd, T. Loret, E. Prats-Alfonso, N. de la Oliva, M. Palma, E. del Corro, M. del Pilar Bernicola, E. Rodríguez-Lucas, T. Gener, J. M. de la Cruz, M. Torres-Miranda, F. T. Duvan, N. Ria, J. Sperling, S. Martí-Sánchez, M. C. Spadaro, C. Hébert, S. Savage, J. Arbiol, A. Guimerà-Brunet, M. V. Puig, B. Yvert, X. Navarro, K. Kostarelos and J. A. Garrido, *Nat. Nanotechnol.*, 2024, **19**, 514–523.
39 Y.-G. Park, S. Kim, S. Min, E. Kim, D. Kim, Y. H. Cho, S. Kim, H. Joo, I. Jeong, J. A. Lim, S. Lee, S.-W. Cho and J.-U. Park, *Nano Lett.*, 2025, **25**, 6481–6490.
40 S. Lee, W. G. Chung, H. Jeong, G. Cui, E. Kim, J. A. Lim, H. Seo, Y. W. Kwon, S. H. Byeon, J. Lee and J.-U. Park, *Adv. Mater.*, 2024, **36**, 2404428.
41 H. I. Ingólfsson, M. N. Melo, F. J. van Eerden, C. Arnarez, C. A. Lopez, T. A. Wassenaar, X. Periole, A. H. de Vries, D. P. Tieleman and S. J. Marrink, *J. Am. Chem. Soc.*, 2014, **136**, 14554–14559.
42 J. S. Choi, H. J. Lee, S. Rajaraman and D.-H. Kim, *Biosens. Bioelectron.*, 2021, **171**, 112687.
43 M. Dipalo, A. F. McGuire, H.-Y. Lou, V. Caprettini, G. Melle, G. Bruno, C. Lubrano, L. Matino, X. Li, F. De Angelis, B. Cui and F. Santoro, *Nano Lett.*, 2018, **18**, 6100–6105.
44 A. Hai, J. Shappir and M. E. Spira, *Nat. Methods*, 2010, **7**, 200–202.
45 I. Engberg, J. A. Flatman and J. D. C. Lambert, *J. Neurosci. Methods*, 1979, **1**, 219–233.
46 F. Pei and B. Tian, *Adv. Funct. Mater.*, 2020, **30**, 1906210.
47 N. Zilinskaite, R. P. Shukla and A. Baradoke, *ACS Meas. Sci. Au*, 2023, **3**, 315–336.
48 B. Gu, Q. Ma, J. Li, W. Xu, Y. Xie, P. Lu, K. Yu, Z. Huo, X. Li, J. Peng, Y. Jiang, D. Li and J. He, *Adv. Sci.*, 2025, **12**, 2407969.
49 H. Teixeira, C. Dias, P. Aguiar and J. Ventura, *Adv. Mater. Technol.*, 2021, **6**, 2000770.
50 S. M. Ojovan, N. Rabieh, N. Shmoel, H. Erez, E. Maydan, A. Cohen and M. E. Spira, *Sci. Rep.*, 2015, **5**, 14100.
51 F. Santoro, J. Schnitker, G. Panaitov and A. Offenhäusser, *Nano Lett.*, 2013, **13**, 5379–5384.
52 B. X. E. Desbiolles, E. de Coulon, A. Bertsch, S. Rohr and P. Renaud, *Nano Lett.*, 2019, **19**, 6173–6181.
53 A. Hai and M. E. Spira, *Lab Chip*, 2012, **12**, 2865–2873.
54 J. Fang, D. Xu, H. Wang, J. Wu, Y. Li, T. Yang, C. Liu and N. Hu, *Nano Lett.*, 2023, **23**, 243–251.
55 Y. Xu, S. Su, C. Zhou, Y. Lu and W. Xing, *Bioelectrochemistry*, 2015, **102**, 35–41.
56 M. S. Saleh, S. M. Ritchie, M. A. Nicholas, H. L. Gordon, C. Hu, S. Jahan, B. Yuan, R. Bezbaruah, J. W. Reddy, Z. Ahmed, M. Chamanzar, E. A. Yttri and R. P. Panat, *Sci. Adv.*, 2022, **8**, eabj4853.
57 M. Dipalo, H. Amin, L. Lovato, F. Moia, V. Caprettini, G. C. Messina, F. Tantussi, L. Berdondini and F. De Angelis, *Nano Lett.*, 2017, **17**, 3932–3939.
58 C. Xie, Z. Lin, L. Hanson, Y. Cui and B. Cui, *Nat. Nanotechnol.*, 2012, **7**, 185–190.
59 D. Xu, J. Fang, M. Zhang, H. Wang, T. Zhang, T. Hang, X. Xie and N. Hu, *Biosens. Bioelectron.*, 2021, **192**, 113501.
60 X. Duan, R. Gao, P. Xie, T. Cohen-Karni, Q. Qing, H. S. Choe, B. Tian, X. Jiang and C. M. Lieber, *Nat. Nanotechnol.*, 2012, **7**, 174–179.
61 Y. Zhao, S. S. You, A. Zhang, J.-H. Lee, J. Huang and C. M. Lieber, *Nat. Nanotechnol.*, 2019, **14**, 783–790.
62 W. G. Chung, E. Kim, Y. W. Kwon, J. Lee, S. Lee, I. Jeong and J.-U. Park, *Adv. Funct. Mater.*, 2024, **34**, 307990.
63 S. Zhao, X. Tang, W. Tian, S. Partarrieu, R. Liu, H. Shen, J. Lee, S. Guo, Z. Lin and J. Liu, *Nat. Neurosci.*, 2023, **26**, 696–710.
64 M. Oh, E. Kim, S.-H. Choi, J. Lee, S. Lee, J. Lee, J. Lee, J.-H. Lee, M. Kwak and J.-U. Park, *ACS Nano*, 2025, **19**, 39464–39479.
65 W. G. Chung, J. Jang, G. Cui, S. Lee, H. Jeong, H. Kang, H. Seo, S. Kim, E. Kim, J. Lee, S. G. Lee, S. H. Byeon and J.-U. Park, *Nat. Nanotechnol.*, 2024, **19**, 688–697.
66 H. Sheng, R. Liu, Q. Li, Z. Lin, Y. He, T. S. Blum, H. Zhao, X. Tang, W. Wang, L. Jin, Z. Wang, E. Hsiao, P. Le Floch, H. Shen, A. J. Lee, R. A. Jonas-Closs, J. Briggs, S. Liu, D. Solomon, X. Wang, J. L. Whited, N. Lu and J. Liu, *Nature*, 2025, **642**, 954–964.
67 J. M. Lee, D. Lin, Y.-W. Pyo, H.-R. Kim, H.-G. Park and C. M. Lieber, *Adv. Sci.*, 2023, **10**, 2300220.
68 Q. Li, K. Nan, P. Le Floch, Z. Lin, H. Sheng, T. S. Blum and J. Liu, *Nano Lett.*, 2019, **19**, 5781–5789.
69 H.-Y. Ahn, J. B. Walters, R. Avila, S. Oh, S. G. Seo, J. U. Kim, J. Park, S. Yoo, Y. S. Choi, T. Y. Kim, J. Liu, J.-Y. Yoo, O. R. Weissleder, D. D'Andrea, C. Park, G. Lee, D. Cho, W.-Y. Maeng, H.-J. Yoon, G. Wickerson, Y. Bouricha, J. Tian, T. C. Chung, S. W. Jordan, S. Li, Y. Huang, C. K. Franz and J. A. Rogers, *Nat. Commun.*, 2025, **16**, 4752.
70 S. Li, D. Lu, S. Li, J. Liu, Y. Xu, Y. Yan, J. Z. Rodriguez, H. Bai, R. Avila, S. Kang, X. Ni, H. Luan, H. Guo, W. Bai, C. Wu, X. Zhou, Z. Hu, M. A. Pet, C. W. Hammill, M. R. MacEwan, W. Z. Ray, Y. Huang and J. A. Rogers, *Sci. Adv.*, 2024, **10**, eadj0268.
71 K. Lim, J. Lee, S. Kim, M. Oh, C. S. Koh, H. Seo, Y.-M. Hong, W. G. Chung, J. Jang, J. A. Lim, H. H. Jung and J.-U. Park, *Nat. Commun.*, 2024, **15**, 7147.
72 P. Le Floch, Q. Li, Z. Lin, S. Zhao, R. Liu, K. Tasnim, H. Jiang and J. Liu, *Adv. Mater.*, 2022, **34**, 2106829.
73 B. W. An, J. H. Shin, S.-Y. Kim, J. Kim, S. Ji, J. Park, Y. Lee, J. Jang, Y.-G. Park, E. Cho, S. Jo and J.-U. Park, *Polymers*, 2017, **9**, 303.
74 Y.-G. Park, S. Lee and J.-U. Park, *Sensors*, 2019, **19**, 4353.
75 J. Chen, K. D. Wise, J. F. Hetke and S. C. Bledsoe, *IEEE Trans. Biomed. Eng.*, 1997, **44**, 760–769.
76 L. Lin and A. P. Pisano, *J. Microelectromech. Syst.*, 1999, **8**, 78–84.

77 J. Scholvin, J. P. Kinney, J. G. Bernstein, C. Moore-Kochlacs, N. Kopell, C. G. Fonstad and E. S. Boyden, *IEEE Trans. Biomed. Eng.*, 2016, **63**, 120–130.
78 E. Kim, W. G. Chung, E. Kim, M. Oh, J. Paek, T. Lee, D. Kim, S. H. An, S. Kim and J.-U. Park, *Small Methods*, 2025, e01227.
79 K. D. Wise, *IEEE Eng. Med. Biol. Mag.*, 2005, **24**, 22–29.
80 E. M. Trautmann, J. K. Hesse, G. M. Stine, R. Xia, S. Zhu, D. J. O'Shea, B. Karsh, J. Colonell, F. F. Lanfranchi, S. Vyas, A. Zimnik, E. Amematsro, N. A. Steinemann, D. A. Wagenaar, M. Pachitariu, A. Andrei, C. M. Lopez, J. O'Callaghan, J. Putzeys, B. C. Raducanu, M. Welkenhuysen, M. Churchland, T. Moore, M. Shadlen, K. Shenoy, D. Tsao, B. Dutta and T. Harris, *Nat. Neurosci.*, 2025, **28**, 1562–1575.
81 J. J. Jun, N. A. Steinmetz, J. H. Siegle, D. J. Denman, M. Bauza, B. Barbarits, A. K. Lee, C. A. Anastassiou, A. Andrei, Ç. Aydın, M. Barbic, T. J. Blanche, V. Bonin, J. Couto, B. Dutta, S. L. Gratiy, D. A. Gutnisky, M. Häusser, B. Karsh, P. Ledochowitsch, C. M. Lopez, C. Mitelut, S. Musa, M. Okun, M. Pachitariu, J. Putzeys, P. D. Rich, C. Rossant, W. Sun, K. Svoboda, M. Carandini, K. D. Harris, C. Koch, J. O'Keefe and T. D. Harris, *Nature*, 2017, **551**, 232–236.
82 H. Shin, Y. Son, U. Chae, J. Kim, N. Choi, H. J. Lee, J. Woo, Y. Cho, S. H. Yang, C. J. Lee and I.-J. Cho, *Nat. Commun.*, 2019, **10**, 3777.
83 R. A. Normann, E. M. Maynard, P. J. Rousche and D. J. Warren, *Vision Res.*, 1999, **39**, 2577–2587.
84 K. Mathieson, J. Loudin, G. Goetz, P. Huie, L. Wang, T. I. Kamins, L. Galambos, R. Smith, J. S. Harris, A. Sher and D. Palanker, *Nat. Photonics*, 2012, **6**, 391–397.
85 M. B. Bhuckory, N. Monkongpitukkul, A. Shin, A. Kochnev Goldstein, N. Jensen, S. V. Shah, D. Pham-Howard, E. Butt, R. Dalal, L. Galambos, K. Mathieson, T. Kamins and D. Palanker, *Nat. Commun.*, 2025, **16**, 2820.
86 P. Li, J. Zhang, H. Hayashi, J. Yue, W. Li, C. Yang, C. Sun, J. Shi, J. Huberman-Shlaes, N. Hibino and B. Tian, *Nature*, 2024, **626**, 990–998.
87 Y. Huang, Y. Cui, H. Deng, J. Wang, R. Hong, S. Hu, H. Hou, Y. Dong, H. Wang, J. Chen, L. Li, Y. Xie, P. Sun, X. Fu, L. Yin, W. Xiong, S.-H. Shi, M. Luo, S. Wang, X. Li and X. Sheng, *Nat. Biomed. Eng.*, 2023, **7**, 486–498.
88 P. Sun, C. Li, C. Yang, M. Sun, H. Hou, Y. Guan, J. Chen, S. Liu, K. Chen, Y. Ma, Y. Huang, X. Li, H. Wang, L. Wang, S. Chen, H. Cheng, W. Xiong, X. Sheng, M. Zhang, J. Peng, S. Wang, Y. Wang and L. Yin, *Nat. Commun.*, 2024, **15**, 4721.
89 J. H. Lee, H. Kim, J. H. Kim and S.-H. Lee, *Lab Chip*, 2016, **16**, 959–976.
90 S. P. Lacour, G. Courtine and J. Guck, *Nat. Rev. Mater.*, 2016, **1**, 16063.
91 F. Fallegger, G. Schiavone and S. P. Lacour, *Adv. Mater.*, 2020, **32**, 1903904.
92 J. Jang, Y.-G. Park, E. Cha, S. Ji, H. Hwang, G. G. Kim, J. Jin and J.-U. Park, *Adv. Mater.*, 2021, **33**, 2101093.
93 J. C. Hwang, M. Kim, S. Kim, H. Seo, S. An, E. H. Jang, S. Y. Han, M. J. Kim, N. K. Kim, S.-W. Cho, S. Lee and J.-U. Park, *Sci. Adv.*, 2022, **8**, eabq0897.
94 H. Yu, W. Xiong, H. Zhang, W. Wang and Z. Li, *J. Microelectromech. Syst.*, 2014, **23**, 1025–1035.
95 G. G. Naples, J. T. Mortimer, A. Scheiner and J. D. Sweeney, *IEEE Trans. Biomed. Eng.*, 1988, **35**, 905–916.
96 C. Dong, A. Carnicer-Lombarte, F. Bonafè, B. Huang, S. Middya, A. Jin, X. Tao, S. Han, M. Bance, D. G. Barone, B. Fraboni and G. G. Malliaras, *Nat. Mater.*, 2024, **23**, 969–976.
97 C. G. Welle, Y.-R. Gao, M. Ye, A. Lozzi, A. Boretsky, E. Abliz and D. X. Hammer, *Biomaterials*, 2020, **238**, 119831.
98 P. R. Patel, E. J. Welle, J. G. Letner, H. Shen, A. J. Bullard, C. M. Caldwell, A. Vega-Medina, J. M. Richie, H. E. Thayer, P. G. Patil, D. Cai and C. A. Chestek, *J. Neural Eng.*, 2023, **20**, 014001.
99 M. Jung, J. Abu Shihada, S. Decke, L. Koschinski, P. S. Graff, S. Maruri Pazmino, A. Höllig, H. Koch, S. Musall, A. Offenhäusser and V. Rincón Montes, *Adv. Mater.*, 2025, **37**, 2418524.
100 J. Abu Shihada, M. Jung, S. Decke, L. Koschinski, S. Musall, V. Rincón Montes and A. Offenhäusser, *Adv. Sci.*, 2024, **11**, 2305944.
101 Q. Huang, B. Tang, J. C. Romero, Y. Yang, S. K. Elsayed, G. Pahapale, T.-J. Lee, I. E. Morales Pantoja, F. Han, C. Berlinicke, T. Xiang, M. Solazzo, T. Hartung, Z. Qin, B. S. Caffo, L. Smirnova and D. H. Gracias, *Sci. Adv.*, 2022, **8**, eabq5031.
102 Y. Park, C. K. Franz, H. Ryu, H. Luan, K. Y. Cotton, J. U. Kim, T. S. Chung, S. Zhao, A. Vazquez-Guardado, D. S. Yang, K. Li, R. Avila, J. K. Phillips, M. J. Quezada, H. Jang, S. S. Kwak, S. M. Won, K. Kwon, H. Jeong, A. J. Bandodkar, M. Han, H. Zhao, G. R. Osher, H. Wang, K. Lee, Y. Zhang, Y. Huang, J. D. Finan and J. A. Rogers, *Sci. Adv.*, 2021, **7**, eabf9153.
103 E. Martinelli, O. Akouissi, L. Liebi, I. Furfaro, D. Maulà, N. Savoia, A. Remy, L. Nikles, A. Roux, L. Stoppini and S. P. Lacour, *Sci. Adv.*, 2024, **10**, eadp8054.
104 Q. Zhao, E. Gribkova, Y. Shen, J. Cui, N. Naughton, L. Liu, J. Seo, B. Tong, M. Gazzola, R. Gillette and H. Zhao, *Sci. Adv.*, 2024, **10**, eadn7202.
105 Y.-G. Park, G.-Y. Lee, J. Jang, S. M. Yun, E. Kim and J.-U. Park, *Adv. Healthcare Mater.*, 2021, **10**, 2002280.
106 J.-H. Kim, S. Kim, J.-H. So, K. Kim and H.-J. Koo, *ACS Appl. Mater. Interfaces*, 2018, **10**, 17448–17454.
107 S. J. French, D. J. Saunders and G. W. Ingle, *J. Phys. Chem.*, 1938, **42**, 265–274.
108 D. Zrnic and D. S. Swatik, *J. Less Common Metals*, 1969, **18**, 67–68.
109 R. Guo and J. Liu, *J. Micromech. Microeng.*, 2017, **27**, 104002.
110 R. Tang, C. Zhang, B. Liu, C. Jiang, L. Wang, X. Zhang, Q. Huang, J. Liu and L. Li, *Biosens. Bioelectron.*, 2022, **216**, 114600.
111 R. Dong, L. Wang, Z. Li, J. Jiao, Y. Wu, Z. Feng, X. Wang, M. Chen, C. Cui, Y. Lu and X. Jiang, *ACS Nano*, 2024, **18**, 1702–1713.
112 Y.-G. Park, H. S. An, J.-Y. Kim and J.-U. Park, *Sci. Adv.*, 2019, **5**, eaaw2844.

113 Z. J. Farrell and C. Tabor, *Langmuir*, 2018, **34**, 234–240.
114 M. J. Regan, H. Tostmann, P. S. Pershan, O. M. Magnussen, E. DiMasi, B. M. Ocko and M. Deutsch, *Phys. Rev. B*, 1997, **55**, 10786–10790.
115 Y.-G. Park, I. Yun, W. G. Chung, W. Park, D. H. Lee and J.-U. Park, *Adv. Sci.*, 2022, **9**, 2104623.
116 S. Kim, J. Lee, W. G. Chung, Y.-M. Hong, W. Park, J. A. Lim and J.-U. Park, *ACS Nano*, 2024, **18**, 24364–24378.
117 M. Kim, J. C. Hwang, S. Min, Y.-G. Park, S. Kim, E. Kim, H. Seo, W. G. Chung, J. Lee, S.-W. Cho and J.-U. Park, *Nano Lett.*, 2022, **22**, 7892–7901.
118 I. Yun, Y. Lee, Y.-G. Park, H. Seo, W. G. Chung, S.-J. Park, J.-W. Cho, J. H. Lee, R. P. Srivastava, R. Kang, B. Lee, D.-Y. Khang, S.-K. Kim, J. H. Noh and J.-U. Park, *Nano Energy*, 2022, **93**, 106857.
119 Y.-G. Park, J. Jang, H. Kim, J. C. Hwang, Y. W. Kwon and J.-U. Park, *Adv. Electron. Mater.*, 2022, **8**, 2101034.
120 Y.-G. Park, H. Min, H. Kim, A. Zhexembekova, C. Y. Lee and J.-U. Park, *Nano Lett.*, 2019, **19**, 4866–4872.
121 H. Moon, J. Kwon, J. Eun, C. K. Chung, J. S. Kim, N. Chou and S. Kim, *Adv. Mater. Technol.*, 2024, **9**, 2301692.
122 D. S. Bassett and O. Sporns, *Nat. Neurosci.*, 2017, **20**, 353–364.
123 K. Deisseroth, *Nature*, 2014, **505**, 309–317.
124 K. Srikantharajah, R. Medinaceli Quintela, K. Doerenkamp, B. M. Kampa, S. Musall, M. Rothermel and A. Offenhäusser, *Sci. Rep.*, 2021, **11**, 18920.
125 G. Rios, E. V. Lubenov, D. Chi, M. L. Roukes and A. G. Siapas, *Nano Lett.*, 2016, **16**, 6857–6862.
126 N. A. Steinmetz, C. Aydin, A. Lebedeva, M. Okun, M. Pachitariu, M. Bauza, M. Beau, J. Bhagat, C. Böhm, M. Broux, S. Chen, J. Colonell, R. J. Gardner, B. Karsh, F. Kloosterman, D. Kostadinov, C. Mora-Lopez, J. O'Callaghan, J. Park, J. Putzeys, B. Sauerbrei, R. J. J. van Daal, A. Z. Vollan, S. Wang, M. Welkenhuysen, Z. Ye, J. T. Dudman, B. Dutta, A. W. Hantman, K. D. Harris, A. K. Lee, E. I. Moser, J. O'Keefe, A. Renart, K. Svoboda, M. Häusser, S. Haesler, M. Carandini and T. D. Harris, *Science*, 2021, **372**, eabf4588.
127 S. Jiang, D. C. Patel, J. Kim, S. Yang, W. A. Mills, Y. Zhang, K. Wang, Z. Feng, S. Vijayan, W. Cai, A. Wang, Y. Guo, I. F. Kimbrough, H. Sontheimer and X. Jia, *Nat. Commun.*, 2020, **11**, 6115.
128 Y. Liu, H. Jia, H. Sun, S. Jia, Z. Yang, A. Li, A. Jiang, Y. Naya, C. Yang, S. Xue, X. Li, B. Chen, J. Zhu, C. Zhou, M. Li and X. Duan, *Nat. Neurosci.*, 2024, **27**, 1620–1631.
129 F. Liu and T.-M. Fu, *NPG Asia Mater.*, 2025, **17**, 32.
130 L. Luan, X. Wei, Z. Zhao, J. J. Siegel, O. Potnis, C. A. Tuppen, S. Lin, S. Kazmi, R. A. Fowler, S. Holloway, A. K. Dunn, R. A. Chitwood and C. Xie, *Sci. Adv.*, 2017, **3**, e1601966.
131 E. Axpe, G. Orive, K. Franze and E. A. Appel, *Nat. Commun.*, 2020, **11**, 3423.
132 Y.-G. Park, Y. W. Kwon, C. S. Koh, E. Kim, D. H. Lee, S. Kim, J. Mun, Y.-M. Hong, S. Lee, J.-Y. Kim, J.-H. Lee, H. H. Jung, J. Cheon, J. W. Chang and J.-U. Park, *Nat. Commun.*, 2024, **15**, 1772.
133 L. Luan, J. T. Robinson, B. Aazhang, T. Chi, K. Yang, X. Li, H. Rathore, A. Singer, S. Yellapantula, Y. Fan, Z. Yu and C. Xie, *Neuron*, 2020, **108**, 302–321.
134 N. Sharafkhani, A. Z. Kouzani, S. D. Adams, J. M. Long, G. Lissorgues, L. Rousseau and J. O. Orwa, *J. Neurosci. Methods*, 2022, **365**, 109388.
135 A. Lecomte, V. Castagnola, E. Descamps, L. Dahan, M. C. Blatché, T. M. Dinis, E. Leclerc, C. Egles and C. Bergaud, *J. Micromech. Microeng.*, 2015, **25**, 125003.
136 C.-H. Chiang, S. M. Won, A. L. Orsborn, K. J. Yu, M. Trumpis, B. Bent, C. Wang, Y. Xue, S. Min, V. Woods, C. Yu, B. H. Kim, S. B. Kim, R. Huq, J. Li, K. J. Seo, F. Vitale, A. Richardson, H. Fang, Y. Huang, K. Shepard, B. Pesaran, J. A. Rogers and J. Viventi, *Sci. Transl. Med.*, 2020, **12**, eaay4682.
137 F. Mazzoni, E. Novelli and E. Strettoi, *J. Neurosci.*, 2008, **28**, 14282–14292.
138 J. L. Stone, W. E. Barlow, M. S. Humayun, E. de Juan Jr and A. H. Milam, *Arch. Ophthalmol.*, 1992, **110**, 1634–1639.
139 Y. Mandel, G. Goetz, D. Lavinsky, P. Huie, K. Mathieson, L. Wang, T. Kamins, L. Galambos, R. Manivanh, J. Harris and D. Palanker, *Nat. Commun.*, 2013, **4**, 1980.
140 D. Palanker, Y. Le Mer, S. Mohand-Said, M. Muqit and J. A. Sahel, *Ophthalmology*, 2020, **127**, 1097–1104.
141 D. Palanker, Y. Le Mer, S. Mohand-Said and J. A. Sahel, *Nat. Commun.*, 2022, **13**, 513.
142 E. Ho, X. Lei, T. Flores, H. Lorach, T. Huang, L. Galambos, T. Kamins, J. Harris, K. Mathieson and D. Palanker, *J. Neural Eng.*, 2019, **16**, 066027.
143 T. Flores, T. Huang, M. Bhuckory, E. Ho, Z. Chen, R. Dalal, L. Galambos, T. Kamins, K. Mathieson and D. Palanker, *Sci. Rep.*, 2019, **9**, 10657.
144 A. Bendali, L. Rousseau, G. Lissorgues, E. Scorsone, M. Djilas, J. Dégardin, E. Dubus, S. Fouquet, R. Benosman, P. Bergonzo, J.-A. Sahel and S. Picaud, *Biomaterials*, 2015, **67**, 73–83.
145 T. Watanabe, H. Kikuchi, T. Fukushima, H. Tomita, E. Sugano, H. Kurino, T. Tanaka, M. Tamai and M. Koyanagi, in *2006 European Solid-State Device Research Conference*, 2006, pp. 327–330.
146 L. Jiang, G. Lu, Y. Zeng, Y. Sun, H. Kang, J. Burford, C. Gong, M. S. Humayun, Y. Chen and Q. Zhou, *Nat. Commun.*, 2022, **13**, 3853.
147 S. Negi, R. Bhandari, L. Rieth, R. Van Wagenen and F. Solzbacher, *J. Neurosci. Methods*, 2010, **186**, 8–17.
148 C. M. Lewis, C. Boehler, R. Liljemalm, P. Fries, T. Stieglitz and M. Asplund, *Adv. Healthcare Mater.*, 2024, **13**, 2303401.
149 S. Arcot Desai, J. D. Rolston, L. Guo and S. M. Potter, *Front. Neuroeng.*, 2010, **3**, 5.
150 E. Bloch, Y. Luo and L. da Cruz, *Ophthalmol. Eye Dis.*, 2019, **11**, 2515841418817501.
151 J. O. Winter, S. F. Cogan and J. F. Rizzo, *J. Biomater. Sci., Polym. Ed.*, 2007, **18**, 1031–1055.
152 J. Lee, S. Kim, W. G. Chung, E. Kim, H. Song, M. Oh, E. Kim, J. Liu, K.-I. Jang, T. Lee and J.-U. Park, *Adv. Eng. Mater.*, 2024, **26**, 2400499.

153 M. A. Lancaster and J. A. Knoblich, *Science*, 2014, **345**, 1247125.
154 H. Clevers, *Cell*, 2016, **165**, 1586–1597.
155 H. Shin, S. Jeong, J.-H. Lee, W. Sun, N. Choi and I.-J. Cho, *Nat. Commun.*, 2021, **12**, 492.
156 J. Cools, Q. Jin, E. Yoon, D. Alba Burbano, Z. Luo, D. Cuypers, G. Callewaert, D. Braeken and D. H. Gracias, *Adv. Sci.*, 2018, **5**, 1700731.
157 D. E. Fullenkamp, W.-Y. Maeng, S. Oh, H. Luan, K. S. Kim, I. A. Chychula, J.-T. Kim, J.-Y. Yoo, C. W. Holgren, A. R. Demonbreun, S. George, B. Li, Y. Hsu, G. Chung, J. Yoo, J. Koo, Y. Park, I. R. Efimov, E. M. McNally and J. A. Rogers, *Sci. Adv.*, 2024, **10**, eado7089.
158 X. Yang, C. Forró, T. L. Li, Y. Miura, T. J. Zaluska, C.-T. Tsai, S. Kanton, J. P. McQueen, X. Chen, V. Mollo, F. Santoro, S. P. Pasca and B. Cui, *Nat. Biotechnol.*, 2024, **42**, 1836–1843.
159 S. O. Sandoval, G. Cappuccio, K. Kruth, S. Osenberg, S. M. Khalil, N. M. Méndez-Albelo, K. Padmanabhan, D. Wang, M. J. Niciu, A. Bhattacharyya, J. L. Stein, A. M. M. Sousa, E. A. Waxman, E. D. Buttermore, D. Whye, C. L. Sirois, S. Anderson, A. Bhattacharyya, E. Buttermore, Q. Chang, D. French, K. Hashimoto-Torii, H. Kornblum, K. Kroll, H. M. Lachman, M. Maletic-Savatic, M. Niciu, B. Novitch, K. Padmanabhan, C. Proschel, M. Sahin, A. Sousa, J. Stein, D. Wang, E. Waxman, D. Whye, A. Williams, X. Zhao, A. Williams, M. Maletic-Savatic and X. Zhao, *Stem Cell Rep.*, 2024, **19**, 796–816.
160 J. Park, J. C. Hwang, G. G. Kim and J.-U. Park, *InfoMat*, 2020, **2**, 33–56.
161 K. Kim, Y.-G. Park, B. G. Hyun, M. Choi and J.-U. Park, *Adv. Mater.*, 2019, **31**, 1804690.